Buoyancy Flux and Mixing Efficiency from Direct, Near-Bottom Turbulence Measurements in a Submarine Canyon

MATTHEW H. ALFORD,[a] BETHAN WYNNE-CATTANACH,[a] ARNAUD LE BOYER,[a] NICOLE COUTO,[a] GUNNAR VOET,[a] CARL P. SPINGYS,[b] BIEITO FERNANDEZ CASTRO,[c] ALEX FORRYAN,[c] ALBERTO C. NAVEIRA GARABATO,[c] AND HANS VAN HAREN[d]

[a] *Scripps Institution of Oceanography, University of California San Diego, La Jolla, California*
[b] *National Oceanography Centre, Southampton, United Kingdom*
[c] *University of Southampton, Southampton, United Kingdom*
[d] *Royal Netherlands Institute for Sea Research (NIOZ), Den Burg, Netherlands*

(Manuscript received 11 January 2024, in final form 13 November 2024, accepted 10 December 2024)

ABSTRACT: Turbulent kinetic energy and thermal variance dissipation rates ϵ and χ, buoyancy flux J_b, diffusivity κ_ρ, and mixing coefficient $\hat{\Gamma} \equiv J_b\,\epsilon^{-1}$, which is simply related to the mixing efficiency $R_f = (1 + \hat{\Gamma}^{-1})^{-1}$, are estimated from highly resolved microstructure measurements collected in a submarine canyon that has been previously shown to be experiencing near-bottom diapycnal upwelling. It is demonstrated that turbulence arises primarily from the convective instability of the internal tide. Twelve tidally resolving stations (12–48 h long) were conducted, wherein profiles were collected from between 5–15 m and 400 m above the bottom every 13–15 min using a custom turbulence vehicle. Turbulent buoyancy flux is estimated using the Osborn and Winters and D'Asaro methods, allowing direct estimation of the mixing coefficient as a function of time, temperature, and height above bottom. Turbulent dissipation and buoyancy flux generally increase toward the seafloor. The associated turbulent diapycnal diffusivity is 10^{-4}–10^{-2} m^2 s^{-1}. Observed $\hat{\Gamma}$ is ~0.2 ± 0.05 near the top of our measurement range, as expected in the ocean interior, and increases to 0.3–0.7 approaching the bottom, consistent with turbulence generated by convective instability.

SIGNIFICANCE STATEMENT: We report detailed direct turbulence measurements very close to the seafloor in a submarine canyon that are well resolved enough in time to confidently understand the processes responsible for the turbulence. We compute the fraction of turbulent power that goes toward mixing, which is an important quantity to understand the role of turbulence in supporting the ocean's large-scale circulation.

KEYWORDS: Abyssal circulation; Diapycnal mixing; Mixing; Thermohaline circulation

1. Introduction

Our understanding of the impact of turbulent mixing on the ocean's general circulation has advanced greatly since the groundbreaking work of Munk (1966). Munk estimated a basin-averaged turbulent diffusivity of approximately 10^{-4} m^2 s^{-4} via a balance between turbulent heat transport and deepwater formation at the poles. Diffusivity was understood to be a proxy for weak interior mixing with turbulent hotspots. The search was then on for whether there was "enough mixing." Work in the 1990s (Munk and Wunsch 1998; Wunsch and Ferrari 2004) took an energetics approach ("Are there enough terawatts?"), noting the inferred total amount of available power for the turbulence (from the winds and the tides). The most recent turn of events has further moved to a watermass modification view ("Can the buoyancy flux divergence affect the needed watermass modification?"). Specifically, St. Laurent et al. (2001), Ferrari et al. (2016), McDougall and Ferrari (2017), and de Lavergne et al. (2016) noted that if turbulent buoyancy flux increases toward the seafloor, then a 1D model implies diapycnal downwelling, not upwelling, which is presumably inconsistent with a steady-state balance. (Munk's constant-diffusivity model obtained upwelling because of the curvature in the ocean's stratification profile.) The apparent paradox may be resolved by allowing upward flow along a sloping seafloor (Ferrari et al. 2016), but observations of such bottom-confined upwelling flows are scarce and the physics driving them is not understood.

The debate, which is well summarized by Polzin and McDougall (2022), is an old one, beginning with early discussions over the nature of the bottom boundary layer (Armi 1978; Garrett 1979). The efficiency of turbulent mixing R_f, which is closely related to the "mixing coefficient" Γ computed here as the ratio of the turbulent buoyancy flux J_b to the dissipation rate ϵ, is intimately wrapped up in all of these discussions. It is often said that Γ is a physically irrelevant quantity, only important in relating ϵ (which we can measure) to the mixing, which we want to know. However, when constraints on the available power for turbulence are known, such as the internal tide conversion rate or the rate of wind work, the mixing efficiency is of fundamental importance because it governs the amount of mixing possible per power (Munk and Wunsch 1998). Since climate simulations are known to be sensitive to modeled variations in Γ (de Lavergne et al. 2016; Cimoli et al. 2019), and Γ may depend on the breaking mechanism of the larger-scale motions, it is well worth studying.

Corresponding author: Matthew H. Alford, malford@ucsd.edu

DOI: 10.1175/JPO-D-24-0005.1

© 2025 American Meteorological Society. This published article is licensed under the terms of the default AMS reuse license. For information regarding reuse of this content and general copyright information, consult the AMS Copyright Policy (www.ametsoc.org/PUBSReuseLicenses).

In the context of the "upside down mixing" paradigm (Ferrari et al. 2016), a one-dimensional balance producing net upwelling near the bottom requires a mixing coefficient below the interior value, which is thought to be 0.2 (Osborn 1980; Ledwell et al. 1993). In a well-mixed boundary layer, this makes sense, but what about in an energetically tidally forced flow with vigorous flushing of the mixed water into the interior?

Substantial evidence supports $\Gamma = 0.2$ in the ocean interior. The first class of evidence is a comparison of diffusivity estimated from direct tracer release and from microstructure estimates (Ledwell et al. 1993; Gregg et al. 2018). The second (e.g., Moum 1996; Monismith et al. 2018; Ijichi et al. 2020) stems from studies that estimate Γ by comparing buoyancy flux from ϵ following Osborn (1980, henceforth O80) and from χ following Osborn and Cox (1972, henceforth OC72). On the other hand, it is known that $|\Gamma| = 1$ ($R_f = 0.5$) in pure convection (Shay and Gregg 1984; Moum et al. 2002; Dalziel et al. 2008; Gayen et al. 2013), since the dominant balance is between dissipation and buoyancy flux. Ijichi et al. (2020) found Γ increasing toward the seafloor, potentially consistent with convective instability playing a greater role near the bottom. Additional evidence from modeling studies of submesoscale flows by Chor et al. (2022) indicates that when symmetric and centrifugal instabilities are at work, Γ might be higher (up to ~0.4), but this has not been observed aside from indirect evidence presented in Spingys et al. (2021) and Cyr and Van Haren (2016). Hence, the dependence of Γ on the breaking mechanism and its variability approaching the seafloor requires more study.

In this study, we use a first-principle rederivation of the Osborn–Cox method (Winters and D'Asaro 1996, henceforth WD96) to compute buoyancy flux on temperature surfaces. While the OC72 and WD96 techniques should be equivalent with enough data, we use WD96 because (i) it is the more fundamental quantity and converges faster since it explicitly targets the diabatic (turbulent) fluxes rather than the internal-wave-driven adiabatic contributions that must be averaged out when using OC72 or correlation methods (Polzin et al. 2021); and (ii) buoyancy flux from WD96 is an intrinsically isopycnal quantity, matching our focus on processes occurring along and across isopycnals in this paper.

Unlike previous statistical studies of Γ such as Moum (1996), Monismith et al. (2018), and Ijichi et al. (2020), the high time resolution of our data allows a process-oriented approach where the breaking events are resolved in time. This ability to glimpse the time evolution of turbulence is aided by our profiler more closely following the flow than most microstructure profilers because the ship was stationary rather than steaming through the water. Ongoing work reported elsewhere will focus on the time-dependent details of mixing efficiency, the ratio of Thorpe and Ozmidov scales, and the buoyancy flux in a reference frame following individual events, for which there is some theoretical context (e.g., Smyth et al. 2001; Mashayek et al. 2021). Here, we describe the phenomenology of the turbulence and the essential physics leading to it and report the bulk profiles of J_b and Γ.

Our study is contextualized by the other measurements made as part of the boundary layer turbulence (BLT) experiment, a multinational effort to address some of the issues described above. The experiment used covariance flux measuring moorings (Polzin et al. 2021), thermistor chain moorings (van Haren et al. 2024), microstructure profiling (this work), and intentional dye and tracer releases in the bottom boundary layer (Wynne-Cattanach et al. 2024). The latter paper demonstrated that diapycnal upwelling is occurring at the time and place of our measurements: (i) a mean up-canyon flow of about 0.02 m s^{-1}, which in steady state must be balanced by diapycnal flow of about 100 m day^{-1}, and (ii) a short-term dye release tracked for 2 days indicating dye crossing isopycnals at approximately the same rate (Wynne-Cattanach et al. 2024). An aim of BLT is to reconcile the observed upwelling with our detailed process observations of turbulence. To preview, we here find $\Gamma = 0.2$ well away from the bottom, increasing to 0.3–0.7 approaching the bottom—possibly consistent with the observed dominance in the region of convective instability, which we demonstrated here is the dominant mechanism. However, Γ never drops below 0.2 near the bottom as expected for a time-invariant 1D bottom boundary layer (Garrett 2001). Likewise, ϵ and J_b generally increase toward the seafloor, as often observed (e.g., Polzin et al. 1997). Hence, a 1D model cannot explain the observed upwelling unless the needed reductions in J_b occur below our measurements, which are often within 5–10 m of the seafloor.

2. Data and methods

a. *The boundary layer turbulence experiment*

The experiment took place in three main cruises in July 2021, October 2021, and July 2022 aboard the British vessel RRS Discovery. The experiment site (Figs. 1 and 2), a submarine canyon in the Rockall Trough off Ireland, was selected for its relatively weak mesoscale eddy field and strong internal tide. Overall, a short-term dye cloud was released in the bottom boundary layer and extensively sampled during the first cruise (Wynne-Cattanach et al. 2024); moorings were deployed on the first cruise, turned around on the second cruise, and recovered on the third cruise (van Haren et al. 2024); a long-term tracer release was conducted on the first cruise and sampled on all three cruises, and turbulence measurements (with a total of four different turbulence instruments) were conducted on all three cruises. These measurements are all discussed elsewhere; the tidally resolving turbulence measurements discussed in this paper were conducted on the first and third cruises.

The submarine canyon occupied during BLT is typical of other submarine canyons (e.g., Petruncio et al. 1998; Lee et al. 2009; Alford and MacCready 2014; Waterhouse et al. 2017) in many regards. Specifically, its thalweg is nearly critical over much of its length with respect to the dominant semidiurnal tides in the region, as shown by the ray (Fig. 2, dashed). Moving inshore, the thalweg becomes supercritical past km 18. At most stations, measured tidally averaged dissipation ϵ increases toward the seafloor (Fig. 2, top), as typically observed (Polzin et al. 1997) and consistent with breaking internal tides

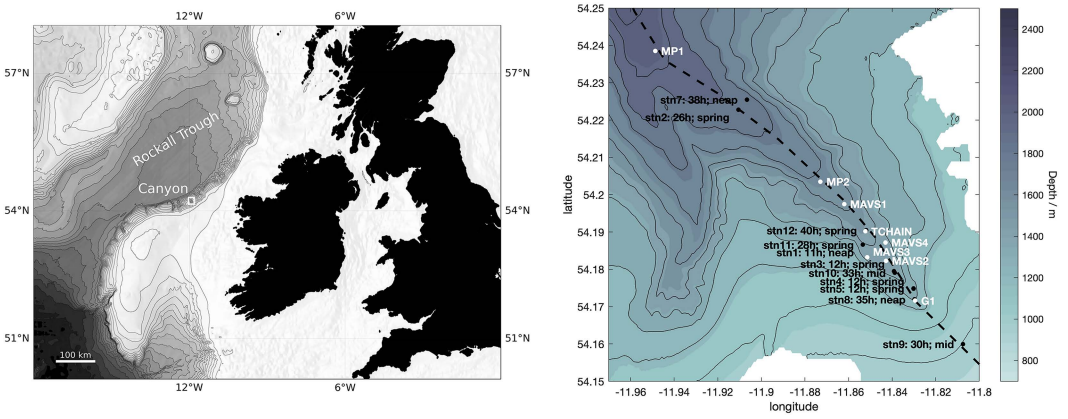

FIG. 1. (left) Overview map showing detailed location plotted at right. Contour spacing is 200 m. (right) Close-up map showing the Rockall Trough bathymetry and the locations of our moorings (white) and epsi-fish stations (black). Station number, time-series length, and spring/neap phase are indicated for each station. Contour spacing is 100 m.

dominating the turbulence. This assertion will be demonstrated clearly in the ensuing time series.

Density in the depth range and region is dominated by temperature (Wynne-Cattanach et al. 2024), with a density ratio $R_\rho \equiv \alpha\theta_z/\beta S_z \approx 2.5 - 5.5$, where α and β are the thermal and haline expansion coefficients, respectively. Additionally, the θ–S curve in the bottom few hundred meters is very tight, indicating minimal large-scale watermass variability and allowing the use of isotherms and isopycnals to be used interchangeably. Hence, we will use isotherms defined by potential temperature θ. However, for these values of R_ρ, unmeasured salinity fluxes can cause temperature-based buoyancy fluxes to be biased high by as much as $R_\rho^{-1} = 25\%$–40%, as discussed in the appendix.

b. *Turbulence profiling*

Turbulence and temperature/salinity profiles were measured with the "epsi-fish" profiler (Fig. 3), a custom vehicle built by the Multiscale Ocean Dynamics (MOD) group at the Scripps Institution of Oceanography, which carries the "epsilometer" turbulence package (Le Boyer et al. 2021), a Seabird Electronics SBE-49 CTD and an altimeter for bottom detections. The instrument uses drag screens to descend at about 0.65 ± 0.05 m s^{-1}.

The epsi-fish instrument is winched up after each profile at approximately 2.5 m s^{-1} with the MOD winch (Fig. 3), a high-speed, direct-drive, autorendering electric winch descended from the fast CTD winch (Klymak et al. 2008) initially built by Rob Pinkel. A 9-m articulating boom ensures the profiler is safely away from the ship's hull and screws while profiling. Because the vehicle falls freely to avoid cable tension that would contaminate turbulence measurements, a powered sheave is employed to pull the cable off the winch drum. Data are telemetered back to the ship in real time up a four-conductor cable with Kevlar braided strength members. As will be discussed below, the epsi-fish is then swept up and down canyon from the ship during each tidal cycle as it profiles the bottom 400 m.

Several modifications to the vehicle, data acquisition system, and standard operating procedure were made for BLT, where we required rapidly repeated profiles from a few hundred meters to just a few meters above the bottom in water depths ranging from 1200 to 2000 m. First, the winch drum was modified for a longer 3000-m cable to account for the deep bottom in the BLT canyon. Second, unlike typical shipboard microstructure profiling where the ship steams ahead of the profiler to ensure it does not surface under the ship, the ship held position in dynamic positioning (DP) mode, minimizing cable payout to ensure the profiler could get to the bottom. Third, the vehicle was modified to clamp the drag screens closed until the vehicle was a few hundred meters off the bottom, when they were opened by sending a "pop the chute" command down the cable to allow normal slow free fall. The increased fall speed during the bulk of the descent further reduced cable payout, increasing the number of profiles that could be made without returning to the surface. Fourth, tethered free-fall profilers require a careful match between payout speed and vehicle fall speed to not only avoid tension on the cable (which contaminates turbulence measurements) but also prevent too much excess cable in the water which can both cause cable-damaging loops and also introduce delays between the winch turning around and the vehicle turning around, leading to bottom impacts. To effect this necessary close match of the two speeds, the number of sheave turns (not the drum, whose relationship with cable payout depends on the amount of cable on the drum) was measured precisely and displayed to the winch operator. Fifth, a crash guard (Fig. 3) was added to protect the probes in case of bottom impacts. Computational fluid dynamics (CFD) and field tests with and without the guard were conducted to ensure vortex shedding from the guard did not contaminate turbulence measurements. Finally, real-time processing allowed an immediate display of acceleration and turbulence quantities to ensure no cable jerks were occurring owing to the tighter-than-usual winch operation.

These improvements to the system, together with the relatively low cost of the vehicle, allowed profiling to be done

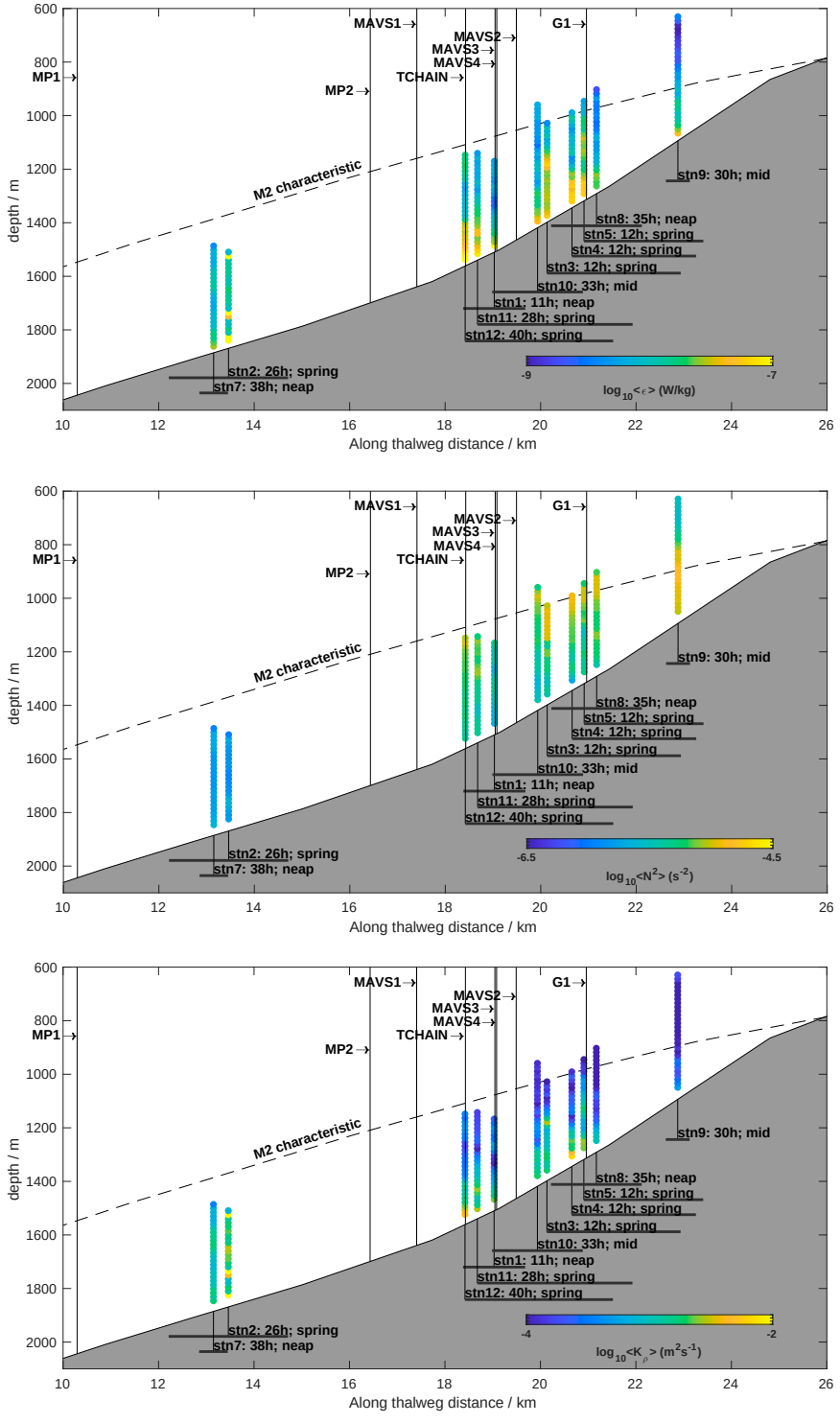

FIG. 2. Cross sections showing the canyon thalweg (Fig. 1; dashed) with mooring (MP1-2, MAVS1-4, and G1, where MP indicates a moored profiler and MAVS moorings are named because they include the Nobska Modular Acoustic Velocimeter which is not used in this study) and epsi-fish station locations (stn1-12). At the top, the station-mean dissipation rate $\langle \epsilon \rangle$ is plotted in color, with a color bar at the lower right. A semidiurnal internal tide ray computed from measured CTD profiles near moored profiler 1 (MP1) is shown in dashed for reference, indicating near criticality and supercriticality on the lower and upper parts of the slope, respectively. Station number, time-series length, and spring/neap phase are indicated for each station. The approximate lateral extent of each station due to tidal advection of the epsi-fish profiler is shown with horizontal gray lines below each station. Colors in (middle) and (bottom) represent stratification N^2 and diffusivity K_ρ, respectively.

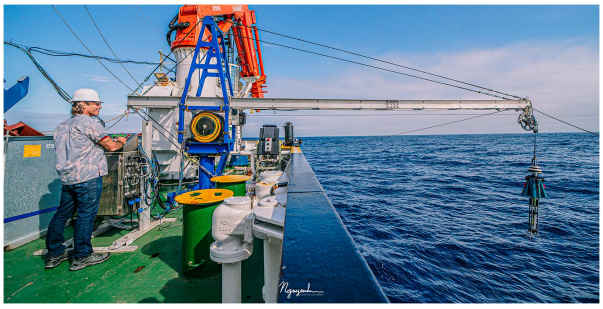

FIG. 3. The MOD winch and the epsi-fish profiler. Photo credit: San Nguyen.

aggressively close to the bottom for such great water depths, with a rapid repeat interval (approximately 14 min). Because the associated Nyquist interval of 28 min is less than the measured buoyancy period at all depths (Fig. 4), the full internal wave field is resolved, and multiple profiles are collected in each turbulent event. At each of the 12 stations, profiles were done from about 400 m from the bottom to 1–20 m from the bottom (Fig. 5)—less for later stations as familiarity increased. The vehicle hit the bottom approximately 20 times during the two cruises with no ill effects to the sensors or the vehicle.

Overall, 1263 profiles were completed on the two cruises, plus approximately 30 other profiles (not reported here) that were not part of tidally resolving time stations. Station location, duration, and spring/neap timing are shown in Figs. 1 and 2. Note that the epsi-fish is swept up and down canyon during each station over a horizontal extent shown by the horizontal gray lines in Fig. 2.

c. *Buoyancy flux and mixing efficiency calculations*

1) COMPUTING ϵ AND χ

We first compute ϵ using best practices from the Analysing ocean turbulence observations to quantify mixing (ATOMIX) working group (Lueck et al. 2024). Shear probes were individually calibrated prior to and after the cruise. The reader is referred to Le Boyer et al. (2021) for details of the ϵ calculation from the epsi-fish. Sample spectra (Fig. 7, left) follow the usual theoretical forms when binned versus ϵ down to the expected noise floor of the instrument of $\approx 2 \times 10^{-10}$ W kg^{-1} (Le Boyer et al. 2021), demonstrating that the atypical profiling techniques described above do not affect the quality of the shear data.

It is well known that the relatively slow response time τ for FP07 thermistors (8.9 ms; Gregg and Meagher 1980) leads to underresolved temperature gradient spectra for typical profiler speeds (e.g., Nash and Moum 2002). For example, the 10% powerpoint at our vehicle's fall speed is 33 cycles per meter. Underresolution increases with ϵ because spectral roll-offs shift to higher wavenumbers for stronger turbulence through the Batchelor wavenumber $k_B \sim \epsilon^{1/4}$, giving rise to potential ϵ-dependent biases in $\hat{\Gamma}$ which is proportional to their ratio (Peterson and Fer 2014; Ijichi and Hibiya 2018).

To account for this effect, we first correct our measured spectra using the Gregg and Meagher (1980) transfer function with $\tau = 8.9$ ms and then compute χ from a model spectrum Batchelor (1967) calculated for the measured ϵ that is fit to the observed spectrum over a wavenumber range 2 cpm $< k < k_{\text{noise}}$. The term k_{noise} is computed as usual as the wavenumber where the measured signal is twice the Johnson noise of the thermistor circuit.

Thermal dissipation rate computed using this method χ_{corr} and from integrating the observed corrected spectrum rather than the model spectrum χ_{raw} agree within 25% above 1100 m where ϵ is $\mathcal{O}(10^{-9})$W kg^{-1}(Figs. 6a,b), but the ratio $\chi_{\text{raw}}/\chi_{\text{corr}}$ drops to 0.3–0.5 below 1100-m depth, where less of the spectrum is resolved because of the greater Batchelor wavenumber where ϵ is $\mathcal{O}(10^{-7})$W kg^{-1}. In spite of the 2–3× magnitude of the corrections on individual χ estimates, they have only a

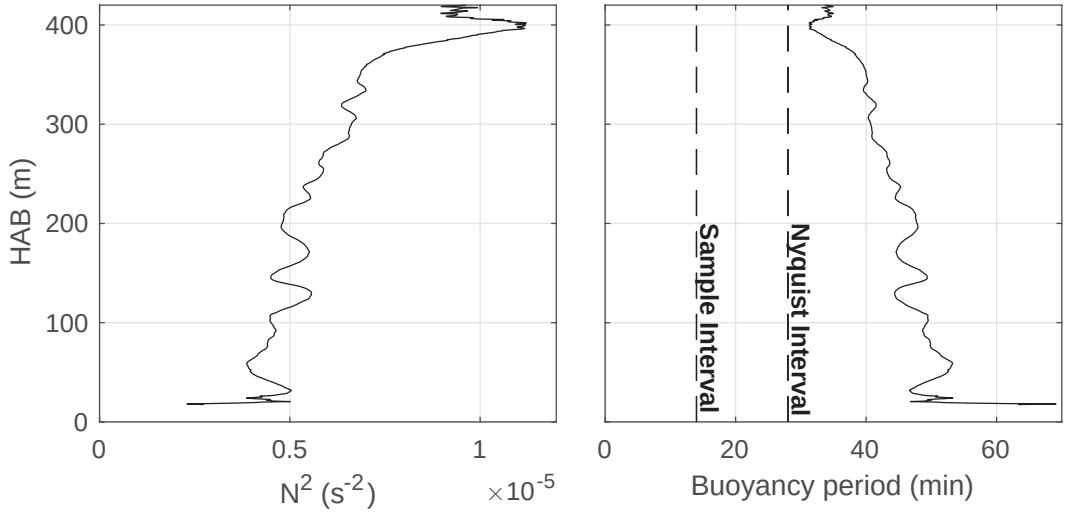

FIG. 4. (left) Measured station-mean buoyancy frequency at station 12. (right) The associated buoyancy period compared to the mean sample and Nyquist intervals of 14 and 28 min, respectively (dashed).

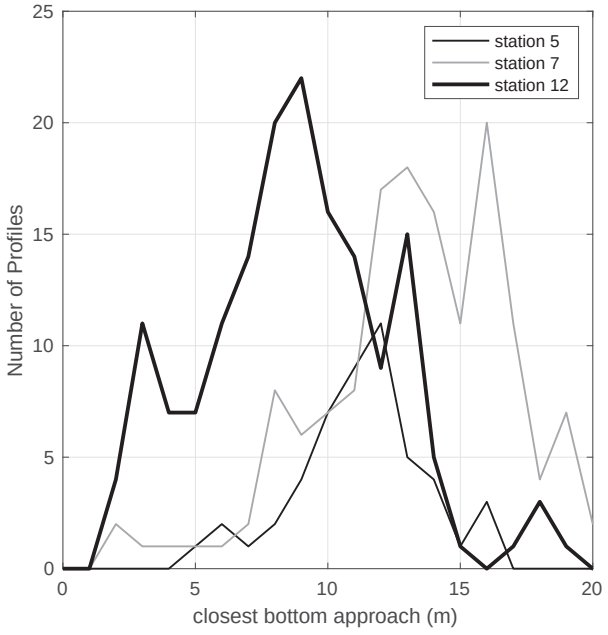

FIG. 5. Histogram of the epsi-fish's closest bottom approach for stations 5, 7, and 12.

modest impact on our estimates of station-mean mixing coefficient.

Since Fig. 6 is a demonstration for a particular patch, we also include a plot with more averaging to demonstrate the quality of the temperature gradient spectra. As also shown in Le Boyer et al. (2021), temperature gradient spectra averaged together for like values of ϵ and χ (Fig. 7, right) follow the expected Batchelor spectrum down to ϵ values near 10^{-10} W kg^{-1}, but noise and sensor response preclude its full resolution as described above. The slight observed elevation of the observed temperature gradient at low wavenumbers could potentially be due to internal wave motions and other "fine structures" that might be expected to be nonturbulent, but the contributions of these low-wavenumber motions to the observed spectra range from only 1.6%–4.4%. Since we integrate the best-fit theoretical spectrum, the potential impact on χ estimates is even less.

For the first three stations, an earlier set of thermistors was used, which turned out to have drift issues that precluded reliable calibrations. Hence, χ (and therefore J_b and Γ) is not computed for those stations.

2) THEORY

We use the diascalar flux formalism and buoyancy flux recipe for vertical profiles of WD96, choosing it over OC72 for the reasons indicated above. The diascalar flux Φ that of potential temperature θ in this case is exactly given by WD96's Eq. (7):

$$\Phi_d = -K\,\frac{dz_*}{d\theta}\langle|\nabla\theta|^2\rangle_{z^*}, \tag{1}$$

where K is the molecular diffusivity of heat, z^* is a diascalar coordinate obtained by three-dimensionally sorting the scalar field to the minimum available potential energy state, and averaging is done along constant values of z^*.

This WD96 estimate of the temperature flux is to be compared with the OC72 expression:

$$J_\theta^{\mathrm{OC72}} = -K\left(\frac{d}{dz}\langle\theta\rangle\right)^{-1}\langle|\nabla\theta'|^2\rangle, \tag{2}$$

where primes represent the fluctuations about a Reynolds average.

As noted in WD96, (1) and (2) involve the scalar flux and have similar forms, but are fundamentally different in that (1) is the diabatic flux alone and therefore must be downgradient; (2) is the vertical flux which includes advective components and therefore can have either sign.

Equation (1) is generally not calculable from observational data owing to the need to sort in three dimensions over the full fluid volume in order to compute z^*. However, WD96 provides a recipe for estimating (6) on a set of j isothermal surfaces θ_j from microstructure data that will converge to (6) for a large number of profiles N:

$$\Phi_d^N(\theta^j) = K\left\langle\frac{dz^*}{d\theta}\right\rangle_j\langle|\nabla\theta|^2\rangle_j. \tag{3}$$

Here, z^* is the sorted vertical coordinate after restoring the potential temperature profile to static stability and $\langle\rangle$ refers to an average over N profiles on each isotherm θ_j. In our data, N ranges from 40 to 160, with averages always encompassing at least one tidal cycle.

The desired buoyancy flux can be computed from the above expressions for temperature flux[1] by taking our standard definitions:

$$\chi \equiv 2K\langle|\nabla\theta'|^2\rangle \quad \text{and} \tag{4}$$

$$J_b \equiv \langle w'b'\rangle = -\frac{g}{\rho}\langle w'\rho'\rangle = -g\alpha\langle w'\theta'\rangle, \tag{5}$$

from which we can finally substitute to get the expressions for the buoyancy flux:

$$J_b^{\mathrm{WD96}}(\theta^j) = \frac{g\alpha}{2}\,\frac{\langle\chi\rangle^j}{\theta_z^*}, \tag{6}$$

where $\langle\chi\rangle$ is the mean thermal dissipation rate on each isotherm j and $\langle\theta_z^*\rangle$ is the mean temperature gradient over N profiles with respect to the vertically sorted diapycnal coordinate z^*.

An analogous estimate of the buoyancy flux from O80 assuming $\Gamma = 0.2$ is given by

$$J_b^{\mathrm{O80}}(\theta^j) = 0.2\epsilon(\theta^j). \tag{7}$$

[1] Unmeasured salinity fluxes can bias temperature-only buoyancy fluxes by as much as R_ρ^{-1}, as discussed in the appendix.

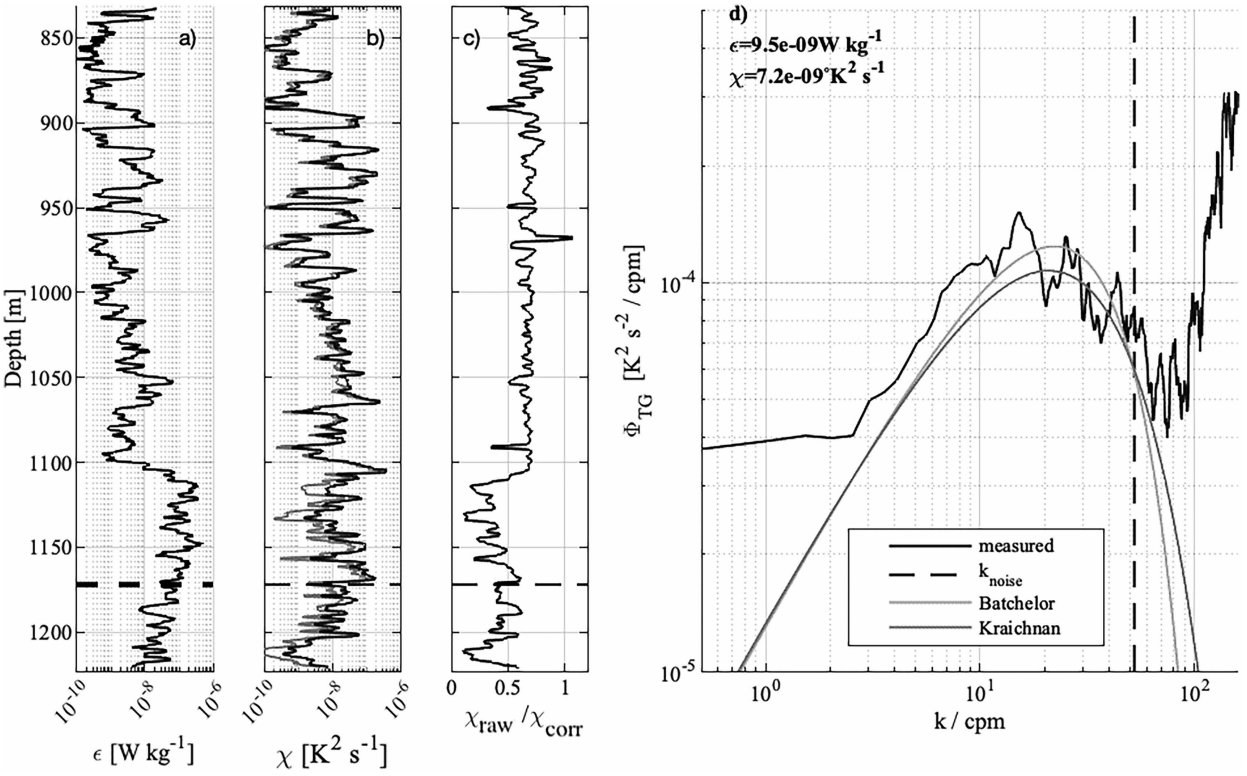

FIG. 6. Demonstration of χ calculation and corrections. (a) An example ϵ profile (station 5; profile 35). The black dashed line in (a)–(c) gives the depth of the spectrum plotted in (d). (b) The term χ estimated from integrating the resolved measured spectrum out to the cutoff wavenumber (gray) and from integrating the theoretical spectrum fitted over the resolved part of the spectrum (black). (c) The ratio of uncorrected to corrected χ. (d) Sample unaveraged temperature gradient spectrum (after time response correction) from the depth indicated in (a)–(c) (dashed) showing the temperature gradient spectrum (black), the cutoff wavenumber k_{noise}, and the best-fit model spectrum (Kraichnan 1968), fitted up to k_{noise} (gray). The Batchelor (1967) and Kraichnan (1968) model spectra are shown for comparison.

If Γ does in fact equal 0.2 and all of our assumptions hold, the two buoyancy flux estimates should be equal. An observational estimate of Γ on each isotherm is then given by

$$\hat{\Gamma}(\theta^j) = \frac{J_b^{\text{WD96}}(\theta^j)}{\langle \epsilon(\theta^j) \rangle}. \tag{8}$$

Moum (1996), Monismith et al. (2018), and Ijichi et al. (2020) all used (8) but with J_b computed from OC72 rather than WD96. With enough data, the two methods should be equivalent.

Finally, mixing efficiency or flux Richardson number, the ratio of buoyancy flux to production, is related to the mixing coefficient Γ via

$$R_f = \frac{1}{1 + \Gamma^{-1}}, \tag{9}$$

as can be easily shown from the well-known expression for time-mean turbulent kinetic energy, production equals buoyancy flux plus dissipation. The term $R_f = J_b P^{-1}$, while $\Gamma = J_b \epsilon^{-1}$. For consistency with past work, we will present estimates of mixing coefficient $\hat{\Gamma}$, where the hat indicates our N-profile observational estimate.

3) CONFIDENCE INTERVALS

Since ϵ, χ, J_b, and $\hat{\Gamma}$ are all approximately lognormal variables, as expected [Gurvich and Yaglom (1993), but see Cael and Mashayek (2021)], confidence intervals are computed following Gregg et al. (1993). Specifically, probability density functions of each quantity are computed in order to estimate the "intermittency" $\sigma_{\ln x}$ for each of the above variables x. The term $\sigma_{\ln x} = 2.0$ for ϵ, χ, and J_b and 1.0 for $\hat{\Gamma}$. The confidence limits for a large number of uncorrelated samples n are then given by Eqs. (17) and (18) of Gregg et al. (1993).

The only art is then in determining the number of uncorrelated samples. To obtain conservative confidence limits, we assumed no additional degrees of freedom were obtained by vertically averaging, since adjacent samples in depth are correlated at scales smaller than 10 m (Gregg et al. 1993). Most microstructure datasets can safely assume successive samples in time are uncorrelated; however, that is not necessarily the case here given the fast profile interval. We therefore assumed a decorrelation time scale of a buoyancy period $2\pi N^{-1}$ and used the rough rule of thumb that $n = N/3$ is one-third the number of profiles N, since we sampled at approximately three times per buoyancy period (Fig. 4). In all cases, n for our stations is large enough to justify the use of the

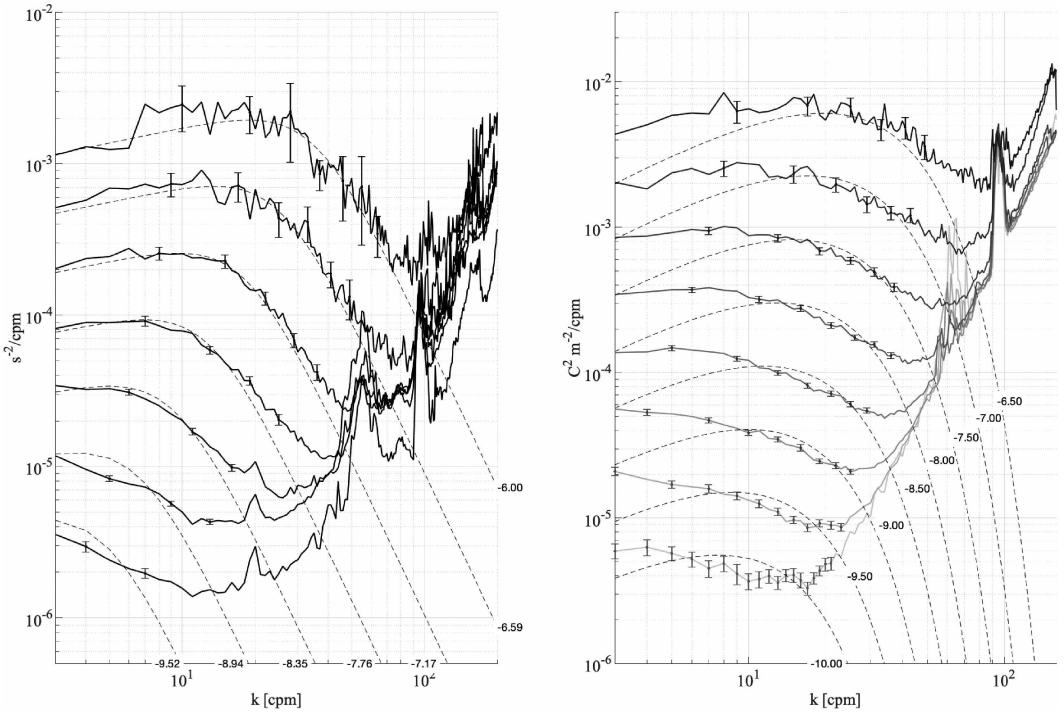

FIG. 7. (left) Wavenumber spectra of shear binned by (black), with Nasmyth (1970) theoretical spectra (dashed). (right) Temperature gradient wavenumber spectra binned by ϵ and (black), with Batchelor (1967) theoretical spectra overplotted (dashed). Error bars are shown for all spectra, and values for ϵ and χ bins are shown at the bottom of each plot.

Gregg et al. (1993) formulas, though only barely in the case of the shortest stations ($N = 48$). Error bars computed using bootstrapping (not shown) gave very similar answers, supporting these assumptions.

3. Results

a. *Time-mean profiles*

Station-mean ϵ profiles (Fig. 2, top) are enhanced toward the bottom, as generally observed (e.g., Polzin et al. 1997). Though not our focus here, a visible enhancement of dissipation rate at repeated nearby stations at spring tide over neap tide is seen (e.g., stations 2/7 and 5/8). In the following, we will present case studies at a critical slope location (No. 7) and two supercritical slope locations (No. 5 and No. 11). As can be seen from Fig. 2, no stations were conducted atop subcritical slopes.

Station-mean buoyancy frequency squared (Fig. 2, middle) shows the general reduction in stratification with increasing depth seen in Fig. 4a. Beyond this tendency, stratification does not decrease near the bottom as expected in 1D analytical solutions of time-mean flow over slopes (e.g., Garrett 2001). Such a lack of reduction in stratification near the bottom has been observed before (e.g., van Haren and Gostiaux 2012).

Station-mean diapycnal diffusivity computed using the O80 formula $\langle \kappa_\rho \rangle = 0.2(\langle \epsilon \rangle / \langle N^2 \rangle)$ (Fig. 2, bottom) shows similar bottom enhancement as seen in ϵ (Fig. 2). Peak values are $\mathcal{O}(10^{-2})\mathrm{m}^2\,\mathrm{s}^{-1}$ near the bottom, decreasing toward the $\mathcal{O}(10^{-5})\mathrm{m}^2\,\mathrm{s}^{-1}$ values expected for the ocean interior (Gregg 1989) near the top of each station. The rough decay scale at most stations is generally 100–400 m [compared with 500 m seen above the Mid-Atlantic Ridge, e.g., Polzin (2009)], but in some profiles (e.g., 2 and 7), our 400-m vertical aperture is not sufficient to see a significant decay.

b. *Station 5 time series*

We first present a 12-h station taken on the supercritical part of the slope (Fig. 8). As stated above, the ship held position at the station location, while the epsi-fish was lowered quickly to a few hundred meters off the bottom. At that point, the "pop the chute" command was sent, allowing the profiler to repeatedly descend slowly until near the bottom. Except for the drag on the line, the profiler essentially follows the lateral flow until its deepest depth when it is rapidly winched up again. As a result, the near-bottom cross-isobath flow sweeps the profiler up canyon over 2 km, so that by 1330 UTC, the water depth below the profiler is only 1200 m (black solid line). Thus, it can be used to infer the phase of the flow even without velocity measurements.

Data are presented both versus pressure (top) and versus height above bottom (bottom). Dissipation rate ϵ (left) is strongly enhanced at the beginning of upslope flow, 0600 UTC, at around 1200 m, and immediately above the bottom near 1030 UTC. Isopycnals (thin black and magenta) are farther apart than average during these periods of elevated ϵ,

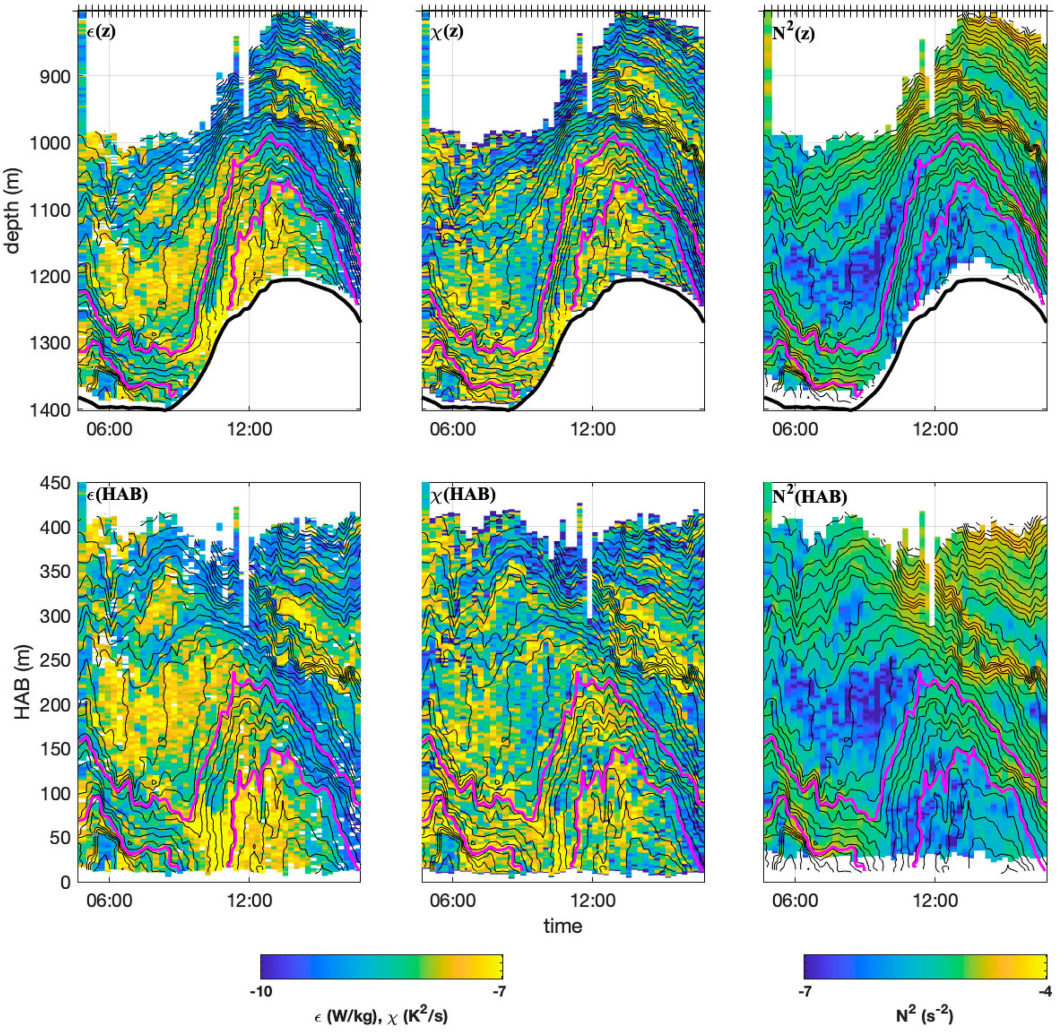

FIG. 8. The (left) ϵ, (center) χ, and (right) N^2 versus (top) pressure and (bottom) height above bottom at station 5, a supercritical location. Isotherms with 20-m mean spacing are plotted in black, while the isotherms 50 and 150 m above bottom on average are plotted in magenta. Profile start times are indicated with ticks at the top. The bottom depth measured from the epsi-fish's altimeter is plotted in (top).

echoing past observations that turbulence occurs when isopycnal strain reduces stratification (Alford and Pinkel 2000; Levine and Boyd 2006). Here, density does not increase monotonically owing to the large statically unstable region, giving multivalued isopycnal depths at those locations. As demonstrated below, convective instability caused by the near-bottom internal tide shear, which is similar to tidal straining in estuaries (Simpson et al. 1990), is the breaking mechanism. By contrast, the later, shallower period of elevated dissipation beginning around 1400 UTC and 300 m above the bottom might be generated by shear instability. Such investigations are the subject of other papers.

The profile interval of 13 min (Fig. 4 and ticks at the top of Figs. 8–10) is rapid enough compared to the flow time scales that the events are well resolved, with multiple profiles through each. Of course, moored estimates from dense thermistor arrays (e.g., van Haren and Gostiaux 2012; van Haren et al. 2024; Voet et al. 2024) are much faster, but do not allow estimation of mixing efficiency.

Thermal dissipation rate χ (middle) shows many of the same patterns, but with the usual tendency to be high in regions of high stratification as expected for a signal involving temperature fluctuations. In fact, the relatively low χ observed in the strong ϵ patches is initially suggestive of a low mixing efficiency due to the weak stratification (right). This naive interpretation will be shown to be incorrect in our direct calculations below.

c. *Station 7 time series*

For comparison, station 7 (Fig. 9), which was taken near neap tide where the slope was nearly critical, shows much smaller vertical excursions of the bottom depth beneath the epsi-fish, owing to both the smaller canyon slope and the

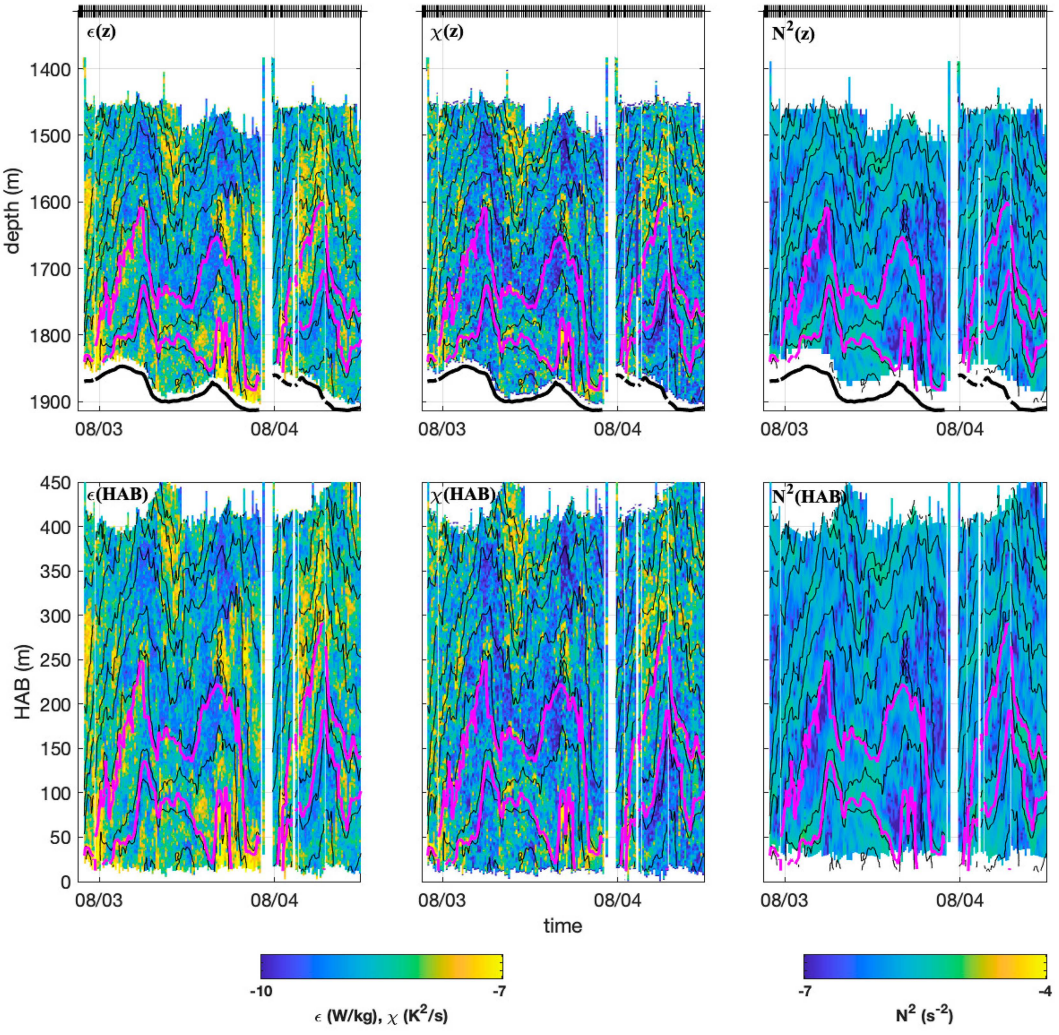

FIG. 9. As in Fig. 8, but for station 7, above a near-critical slope.

weaker neap-tide flows. Isopycnal displacements are similar to station 5, but turbulence is significantly weaker. The phasing of the turbulence with respect to the up-canyon flow is delayed somewhat relative to the last station, occurring slightly after peak up-canyon flow. This phase shift, which is also seen at the other near-critical stations (not shown), is the main qualitative difference between the near- and supercritical stations.

d. Station 12 time series

The longest and nearest-to-the-bottom station (Fig. 10) was collected near spring tide. This 40-h station, most of whose profiles are <10 m above bottom, shows clearly enhanced ϵ and χ and large vertical isopycnal displacements. Lateral excursions of the epsi-fish were strong, resulting in over 250-m difference in the profile depth between maximum up- and down-canyon tidal phases. While the long time series provides good statistics for the buoyancy flux calculations to be presented next, a 12-h zoom (Fig. 11) is more useful for showing the processes involved and the turbulence details. Now, similarly enhanced turbulence, which again appears convective in nature owing to the vertical and multivalued isopycnals in the lower 50 m or so, is observed during up-canyon flow. However, at this station, turbulence is also enhanced on the down-canyon flow, unlike most other stations. This pattern is seen on the other tidal cycles measured at station 12 (Fig. 10), as well as at nearby station 11.

e. Canyon dynamics and breaking mechanism

Having presented the basic time series of ϵ, χ, and N^2 at our three sample stations 5, 7, and 12, we now present a detailed comparison of three stations (3, 4, and 5) that were near the MAVS2 mooring at 19.5 km (Fig. 2). We do this comparison now before proceeding to the buoyancy flux and mixing coefficient calculations in order to demonstrate that convective instability by differential advection is the dynamical mechanism leading to the observed near-bottom turbulence.

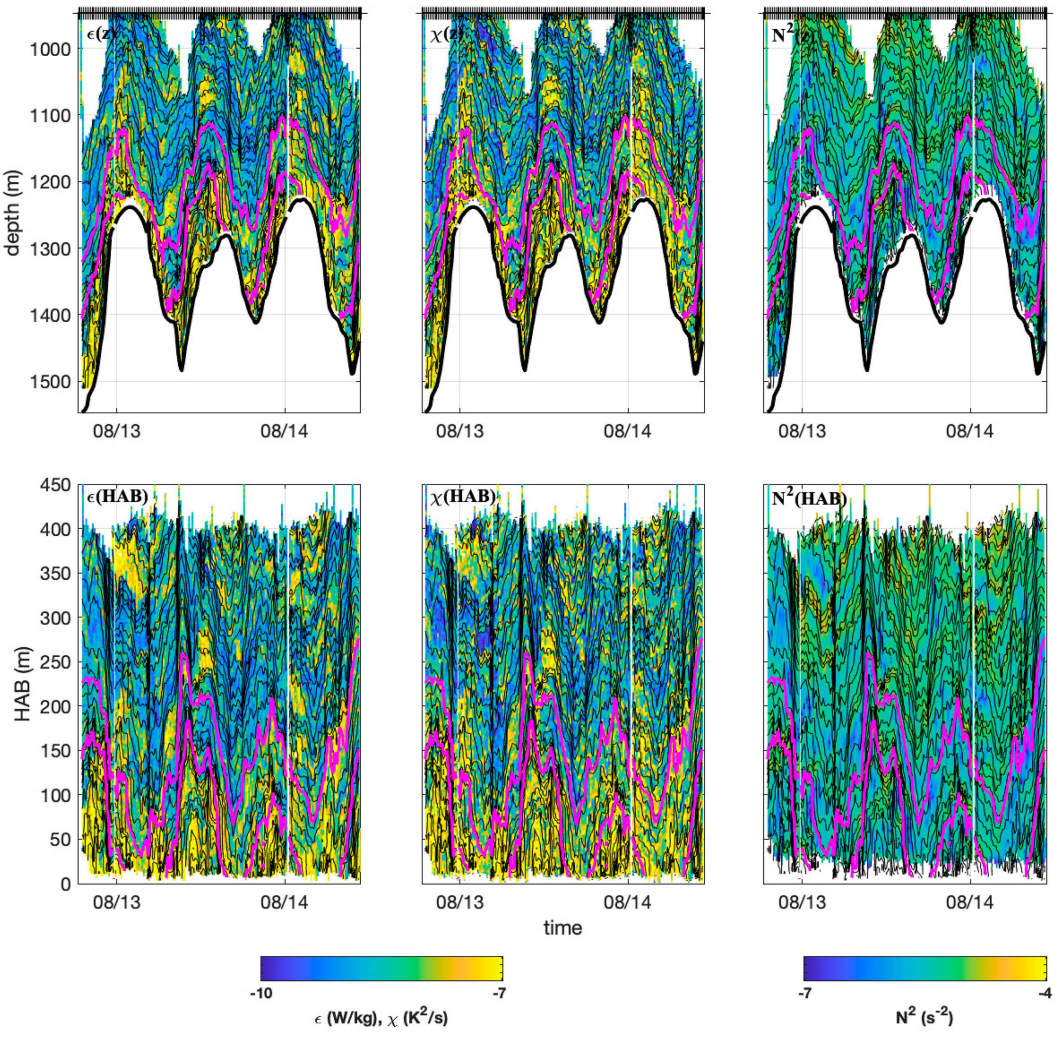

FIG. 10. As in Fig. 8, but for station 12, a supercritical location.

As was true for each of the three previous stations, up-canyon velocity (Fig. 12a) is associated with a reduction in N^2 (Fig. 12b) and heightened ϵ (Fig. 12c). As pointed out in van Haren et al. (2024), the flow 100–200 m above the bottom exceeds that nearer to the bottom. Assuming the flow near the bottom is parallel to the bottom, this sheared-up-canyon flow sweeps denser fluid above lighter fluid, leading to statistically unstable conditions that result in convective instability. The mechanism is the same as demonstrated in a lake by Lorke et al. (2005), but here the near-bottom shear extends not over ~2 m as in their study but over 100–200 m, a region far too thick to be a frictional boundary layer. Rather, the reduction in near-bottom velocity is consistent with the form drag of a propagating internal gravity wave encountering the slope. Though it is beyond the scope of this work, the horizontal and vertical structures of the semidiurnal velocities are consistent with a low-mode internal Kelvin wave (K. Polzin 2023, personal communication).

Taking the depth mean of each quantity over the bottom 100 m (Fig. 13), it is clear for stations 4 and 5 that depth-mean stratification begins to drop (Fig. 13b) and depth-mean ϵ (Fig. 13c) begins to rise immediately when the differential flow (flow near 100 m minus the bottommost measurement; thick line) becomes positive, as expected for the differential advection mechanism. Station 3 does not show strong modulation in either N^2 or ϵ, possibly because the station began after the turbulence began.

We interpret the observed reduction in stratification as evidence that convective instability produced by differential internal tide advection has led to the observed turbulence, as demonstrated previously over other slopes (Hosegood et al. 2005; Alford et al. 2011). To prove this assertion quantitatively, we follow Moum et al. (2004), Lorke et al. (2005), and Ruan et al. (2019) in computing the destabilizing buoyancy flux associated with the differentially advected flow. We consider a flow difference Δu over a vertical distance H over a bottom with slope β. If the near-bottom flow is parallel to the bottom, then the along-slope density gradient equals the vertical gradient times the bottom slope $\partial\rho/\partial x = \beta(\partial\rho/\partial z)$. Then, the destabilizing buoyancy flux due to differential advection equals

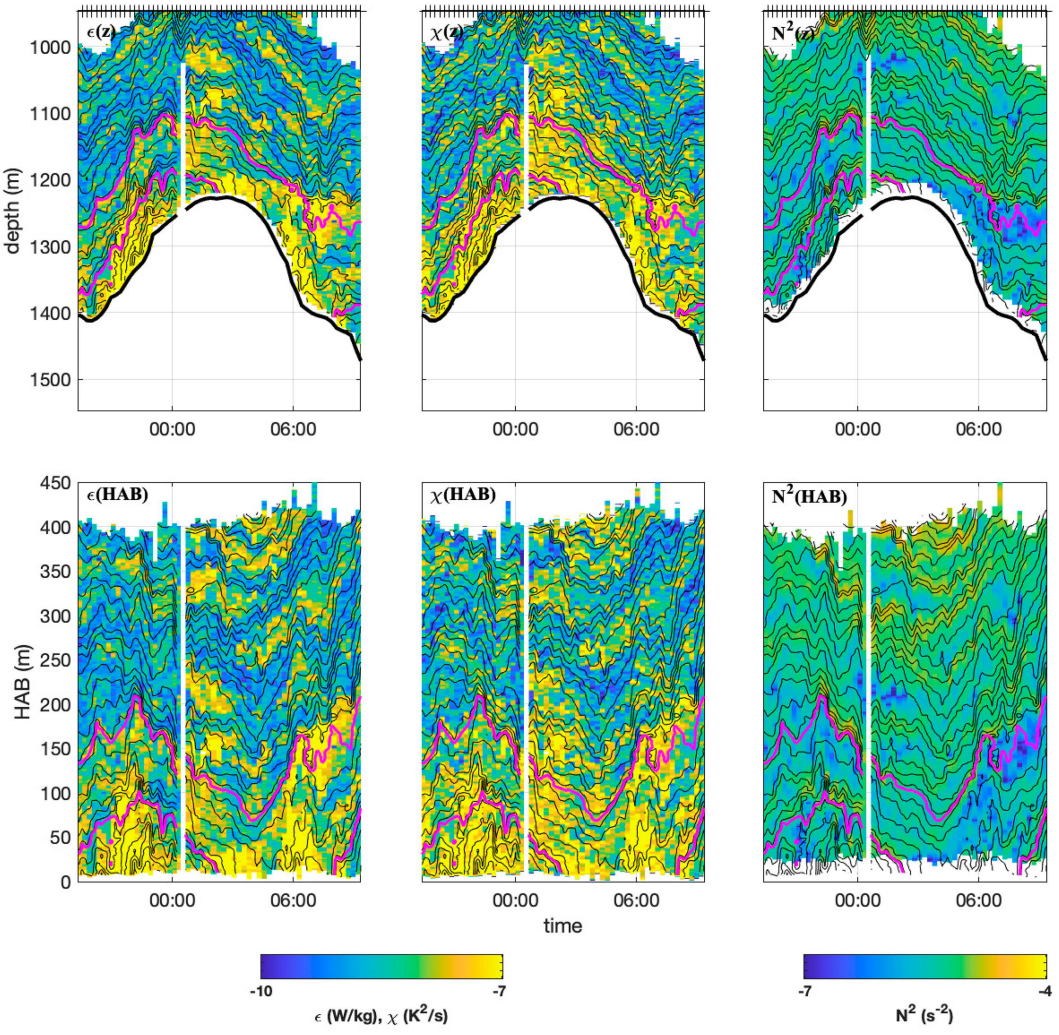

FIG. 11. As in Fig. 10, but zoomed in to a 12-h period near 14 Aug.

$$J_b^{\mathrm{adv}} = \frac{g}{\rho_o} H \Delta u \beta \frac{\partial \rho}{\partial z}. \tag{10}$$

If convective instability rather than shear instability is the energy source for the turbulence, then $J_b^{\mathrm{adv}} = \epsilon$, in contrast to the three-term "production equals dissipation plus buoyancy flux" balance $P = J_b - \epsilon$ expected for shear instability where production is the energy source. As discussed, in this situation, a mixing coefficient of 1 is expected as described above since $J_b = \epsilon$.

The time rate of change of the stratification $\partial(N^2)/\partial t$ equals

$$\frac{\partial(N^2)}{\partial t} = \frac{J_b^{\mathrm{adv}}}{H^2}. \tag{11}$$

Taking values $g = 9.8\ \mathrm{m\ s^{-1}}$, $\rho_o = 1026\ \mathrm{kg\ m^{-3}}$, $H = 100$ m, $\beta = 0.08$, and an initial stratification of $N_o^2 = 4 \times 10^{-6}\ \mathrm{s^{-2}}$, as observed, the predicted stratification rate at stations 4 and 5 (Fig. 13b, dashed) agrees very well with the observed reduction in both timing and magnitude.

The timing of the advective destabilizing buoyancy flux agrees very well with the observed depth-mean ϵ at stations 4 and 5 (Fig. 13c). At station 3, as stated above, near-bottom ϵ at station 3 does not show a marked peak. The phase agreement at stations 4 and 5 provides more support for the convective instability mechanism as the source of the turbulence. However, J_b^{adv} is 5–20 times larger than measured ϵ, which demonstrates that the advective destabilizing buoyancy flux provides more than enough to explain the observed turbulence.

There are several reasons for the possible excess. First and likely most important, a portion of the destabilizing buoyancy flux is likely to be adiabatic. This reversible part of the increase in potential energy may be returned on the next tidal swing rather than going into turbulence. Second, cross-canyon differences in any of the terms going into computing the advective buoyancy flux and/or measured ϵ could be responsible. Third, the advective buoyancy flux process should reduce the lateral stratification over time in proportion to the observed reduction in vertical stratification; however, we have

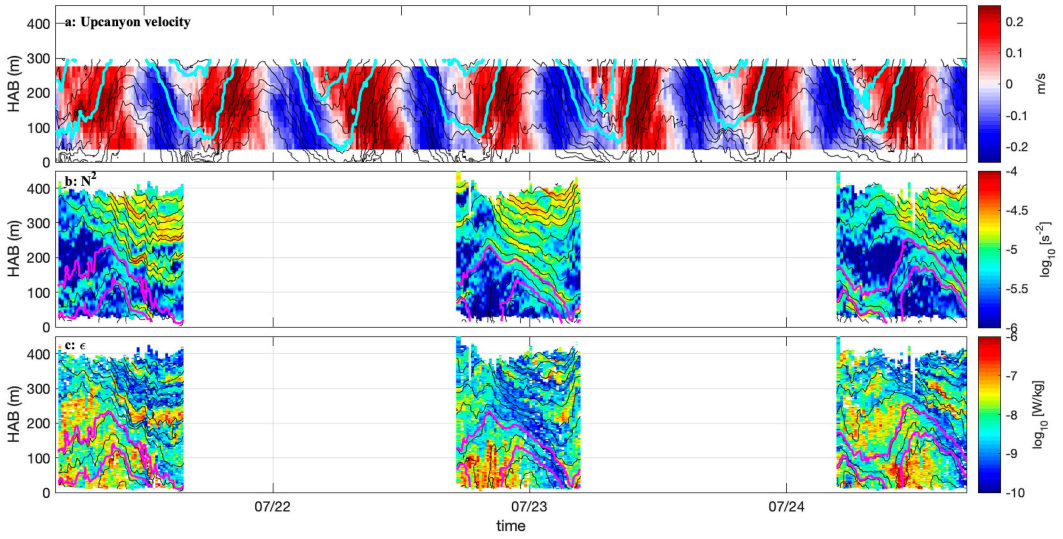

FIG. 12. (a) Up-canyon velocity versus height above bottom measured from an up-looking Teledyne RD Instruments (TRDI) ADCP on the MAVS2 mooring (location in Figs. 1 and 2). (b) Stratification, N^2, measured at epsi-fish stations 3, 4, and 5, which were just up-canyon from the mooring (Fig. 2). (c) As in (b), but for ϵ. Isotherms spaced every 0.1°C are overplotted in all panels. Cyan lines in (a) indicate the 5.22° and 5.75°C isotherms, which are on average 50 and 150 m above bottom, respectively. The same two isotherms from (a) (cyan) are contoured in (b) and (c) in magenta.

not accounted for this reduction owing to the uncertainties and assumptions in estimating the lateral gradients from this simple formula. Fourth, the buoyancy flux provides the potential energy for the convective instability and hence should be related to the outer scale of the turbulence, which might be expected to be related to the Thorpe scale (Dillon 1982). It has been argued before that early on in the development of turbulence, the Thorpe scale exceeds the Ozmidov scale, so that estimates of ϵ from Thorpe scales exceed directly measured ϵ by factors of 5–10 (Mater et al. 2013, 2015), similar to the difference seen here between J_b^{adv} and ϵ. We do indeed see a similar excess in Thorpe-inferred and directly measured ϵ (A. Le Boyer et al. 2025, unpublished manuscript), consistent with this interpretation. Such behavior is generally expected in early turbulence where static instabilities have been created but have not fully developed into turbulence (Smyth et al. 2001; Mashayek et al. 2021). Hence, it may be that the destabilizing buoyancy flux has created a static instability that has begun to be turbulent, but will not fully convert its potential energy into dissipation until further up canyon.

f. *The epsi-fish's reference frame*

We here make an effort at determining the degree to which the profiler follows the flow. Untethered profilers are known to follow the background flow on scales larger than the vehicle length very well (e.g., Hayes et al. 1984), but the added drag of a long tether adds uncertainty. For stations 3, 4, and 5, which were very close to the MAVS2 mooring, we compute the mean up-canyon velocity over the mooring's full extent, 30–280 m above bottom, and integrate it in time to obtain the up-canyon displacement a perfect flow follower would go. Though we did not acoustically track the epsi-fish's trajectory, it is straightforward to compute its along-canyon distance assuming it remains on the thalweg from the closest bottom approach for each profile (measured as the maximum instrument depth plus the altimeter distance to the bottom) by the bottom slope, estimated from the bathymetry at that location. In spite of some differences at station 3 (Fig. 14), good agreement is seen, suggesting the vehicle does follow the flow to a large degree. Sources of error include the lack of velocity measurements from 280 to 400 m above bottom, along-canyon variability in currents, changes in bottom slope, and vertical shear.

The effect of the epsi-fish's moving reference frame is also evident in temperature, as seen by comparing the isotherms observed at the mooring (Fig. 12a) and at the epsi-fish stations. The cyan contours in Fig. 12a are the same potential temperature values, 5.22° and 5.75°C, as the magenta curves in Figs. 12b and 12c. The two isotherms appear higher above the bottom at MAVS2 because it is in deeper water than the epsi-fish stations. More importantly, the vertical excursions are much greater in Fig. 12a than in Figs. 12b and 12c because the epsi-fish follows the flow to the degree just demonstrated. Of course, if it were perfectly Lagrangian and there were no shear, isotherms in Figs. 12b and 12c would remain flat. Instead, isotherms observed by the epsi-fish are observed to rise and fall on up-canyon and down-canyon flows, respectively, consistent with the epsi-fish moving up canyon slightly slower than the depth-mean flow.

g. *Buoyancy flux and mixing efficiency calculations*

Our calculations of J_b and $\hat{\Gamma}$ are presented beginning with station 5 (Fig. 15). At the upper left, buoyancy flux from the O80 method (i.e., 0.2ϵ) is plotted versus potential temperature

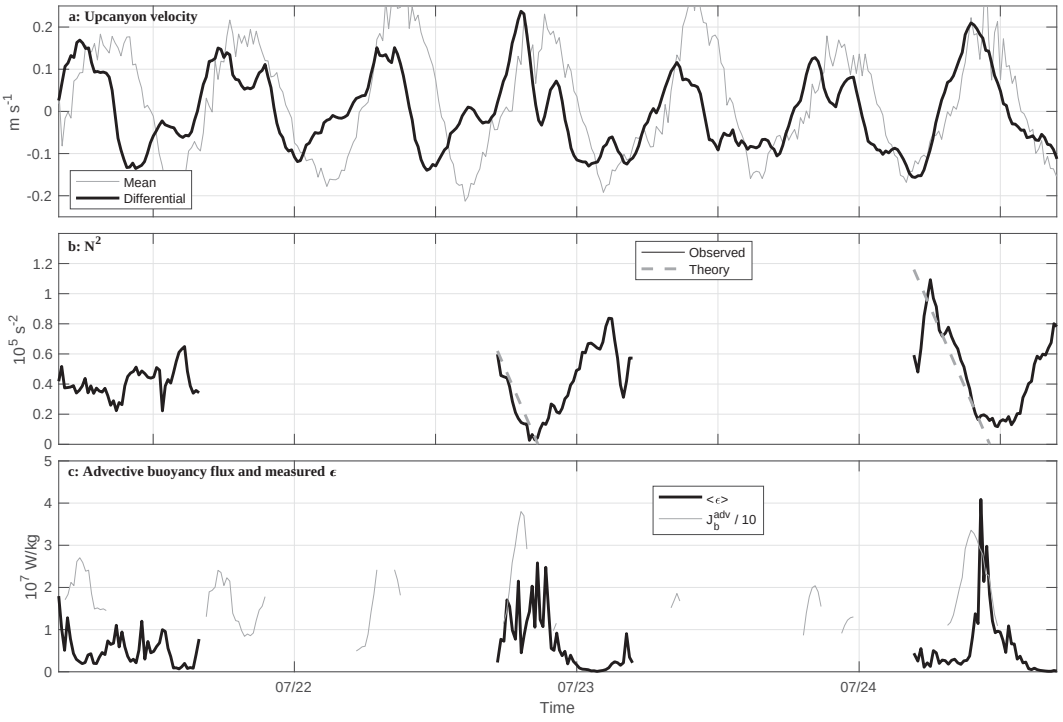

FIG. 13. (a) Up-canyon velocity computed as the depth mean over the bottom 100 m (thin) and as the difference between velocities at 100 and 25 m, the closest measurement to the bottom (thick). (b) The term N^2 averaged over the bottom 100 m from each epsi-fish station (thick). The destratification rate $\partial(N^2)/\partial t$ from (11) is overplotted for stations 4 and 5 (dashed). (c) The term ϵ averaged over the bottom 100 m from each epsi-fish station (thick) and (thin gray) one-tenth the advective destabilizing buoyancy flux J_b^{adv} [(10)].

and time. At the upper center, the equivalent quantity computed using WD96 [(6)] with $N = 1$ is plotted using the same color axes. In each panel, the rise and fall of temperature surfaces seen in Fig. 8 are now evident as the appearance and disappearance of those isotherms from our record either from the top or the bottom. That is, the values with white immediately below are those closest to the seafloor. Some distortion of the water column is inherent in such a temperature-coordinate view (Pinkel et al. 1991), since regions of relatively weak stratification occupy a large physical volume but only have a few isotherms. The magenta isotherms plotted before now appear as horizontal lines. The region of very strong dissipation and mixing in Fig. 8 can be seen beginning with water near 6°C, moving to cooler and cooler water as time progresses. Buoyancy flux computed using the O80 and WD96 methods gives similar values, because the weaker stratification is accounted for in (6), which is remarkable given that no averaging has been done for either calculation.

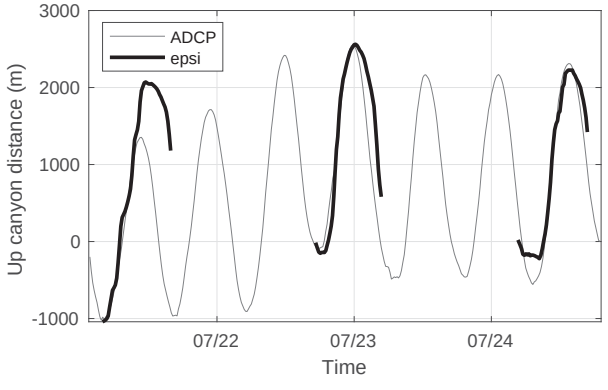

FIG. 14. Up-canyon displacement of the epsi-fish at stations 3, 4, and 5 (heavy) and the integrated depth-averaged, de-meaned velocities from the nearby MAVS2 mooring (thin).

If Γ were uniform and 0.2 everywhere and at all times, the upper left and center panels of Fig. 15 would be identical. In reality, differences are seen, but they do not conspire to modulate $\hat{\Gamma}$ more than a factor of 2 or so. Given the assumptions and averaging assumed in both the O80 and WD96 methods, the qualitative degree of agreement at individual times and depths is remarkable. These statements are made quantitative first by computing the time-mean values of J_b from each method along each isotherm (lower left); $\hat{\Gamma}$ (lower center) is then simply the ratio of $J_b^{\mathrm{WD96}}/\epsilon$. Though it makes little quantitative difference, we note that N-profile averages are computed on each isopycnal before ratios are taken, following (6) and (8). That is, mean J_b is not the same as the isopycnal average of all of the J_b values plotted in the top row (which have $N = 1$). As described above, 95% confidence limits on $\hat{\Gamma}$ are estimated from the number of profiles N (lower right, red), which depends on temperature as isotherms enter and exit

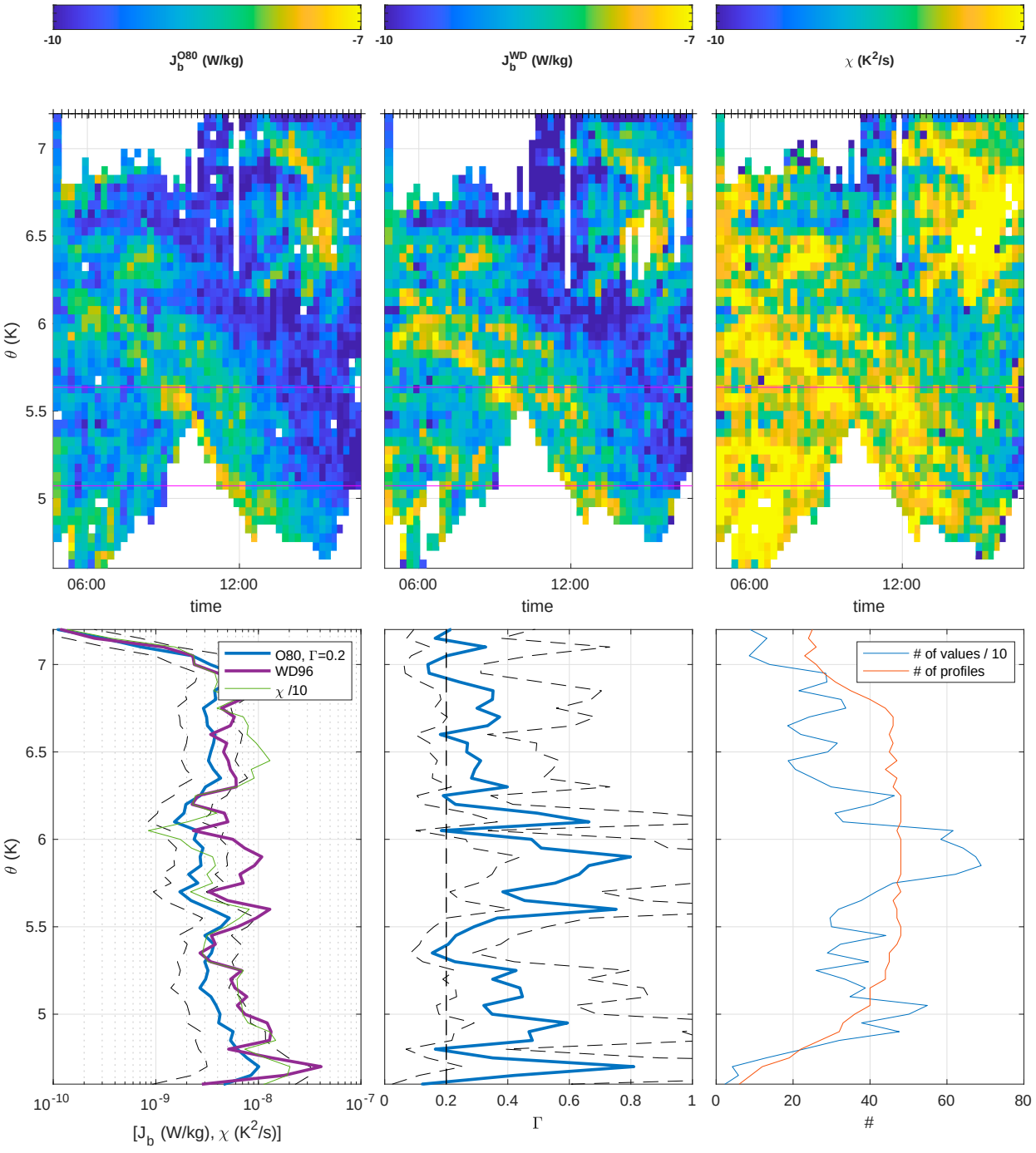

FIG. 15. Buoyancy flux for station 5: (top left) J_b versus temperature and time from O80, (top center) J_b versus temperature and time from WD96, and (top right) χ versus temperature and time. Horizontal magenta lines are the isotherms plotted in the previous figures, and profile times are indicated at the top with ticks. (bottom left) Station-mean J_b from each method. Station-mean χ is plotted in gray for reference, divided by 10 to fit on the plot. Error bars computed as in the text are plotted for the O80 estimate (dashed); error bars for the other quantities are identical. (bottom center) Mixing coefficient $\hat{\Gamma}$ versus temperature, with error bars (dashed) computed as in text. The vertical dashed line indicates the O80 value of 0.2. (bottom right) The number of profiles (red) and the number of ϵ and χ measurements going into each J_b estimate (divided by 10 to fit on the plot).

our vertical profiling range as shown in the leftmost two panels. The number of raw 1-m ϵ and χ samples going into each average is also shown (lower right, blue; divided by 10 to fit on the plot). As expected, confidence drops on the warmest and coldest isotherms in the vertical profiling range owing to fewer profiles reaching those temperatures, as can be seen in the two rows.

Observed mixing coefficient $\hat{\Gamma}$ increases moving to colder (deeper) water, but is only statistically different from 0.2 (dashed) between θ = 5.6°–6°C and 4.8°–5°C at this station, consistent with the good agreement in the depth profiles of J_b^{WD96} and J_b^{O80} (bottom left). (Error bars are relatively large given the short station duration.) Both buoyancy flux estimates are enhanced relative to the warmest water sampled at the station but increased only slightly toward the bottom. Station-mean χ is also plotted for comparison (gray), divided by 10 to fit on the plot.

At the deeper, near-critical station 7 (Fig. 16), the close agreement is once again seen in the patterns of buoyancy flux estimated using the O80 and WD96 methods, but the time-mean buoyancy flux from WD96 (lower left, purple) exceeds that computed from O80 (blue) at all depths. Correspondingly, $\hat{\Gamma}$ hovers between 0.4 and 0.6, only decreasing to 0.2 closer to the bottom, in contrast to the supercritical stations. This station proves to be an anomaly from the other stations, leading us to speculate if mixing efficiency over near-critical slopes might be greater than over supercritical ones. Unfortunately, the FP07 sensors on the other near-critical station 2 had poor calibrations, and so we cannot reproduce this result from that station.

Finally, station 12 (Fig. 17) shows similar buoyancy flux and mixing coefficient patterns as station 5. The Hovmöller plots once again show a close match between buoyancy flux patterns computed using the two methods (upper left and upper center). Time-mean buoyancy flux (lower left, purple and blue) matches closely on warmer isotherms, but the WD96 estimate exceeds the O80 estimate by approximately a factor of 2 at depth. Consistent with expectations for the ocean interior as described in the introduction, $\hat{\Gamma}$ (bottom center) is ≈0.2 for $\theta > 7$°C, increasing to 0.4–0.6 on deeper isotherms. Because of the longer time series, error bars for stations 7 and 12 are tighter than for station 5.

We conclude by plotting all station-mean profiles, and the mean over all stations, of $\hat{\Gamma}$ computed identically as for the three example stations shown (Fig. 18). Profiles are plotted versus height above bottom using the mean height above bottom of each isotherm plotted previously. With the exception of the near-critical station 7, all profiles show similar behavior as stations 5 and 12 which were described in detail above, with $\hat{\Gamma}$ close to 0.2 aloft and increasing to 0.3–0.7 approaching the seafloor. At no station does mixing efficiency decrease below 0.2 approaching the bottom.

4. Summary and discussion

This paper has used 12 highly resolved microstructure stations, spanning 1–4 tidal cycles each, to compute the kinetic energy and thermal variance dissipation rates, buoyancy flux, diffusivity, and mixing efficiency in a submarine canyon that is known to be undergoing diapycnal upwelling (Wynne-Cattanach et al. 2024) and convective instability, as shown here. The physical processes that conspire to give upwelling, when turbulence increases toward the seafloor and therefore would give downwelling in a 1D model, are discussed in Garabato et al. (2024, manuscript submitted to *Nat. Geosci.*). The degree to which these results are generalizable to other canyons and sloping regions of the ocean's bottom remains an open question. However, for our canyon at least, our work appears to rule out one explanation of the phenomena suggested in St. Laurent et al. (2001), namely, that Γ goes to zero in a broad bottom boundary layer (300 m thick in their inverse). To the contrary, our data indicate that if anything, Γ increases toward the seafloor. Of course, we can make no statements about the bottom 0–10 m where we have little data. On the other hand, the upwelling in our canyon observed by Wynne-Cattanach et al. (2024) extended much higher above the seafloor than 10 m. Further work should prioritize understanding the generalizability of our results to larger-scale regions such as the Brazil basin (Polzin et al. 1997) and the abyssal circulation in general.

Hence, our observed buoyancy flux profiles generally increase toward the seafloor, which would give downwelling in a 1D model, not upwelling. Even assuming a constant buoyancy flux in a canyon with an area shrinking toward the seafloor as did Kunze et al. (2012), the resultant upwelling is 100 times smaller than documented by a dye release (Wynne-Cattanach et al. 2024). The slight decrease in $\hat{\Gamma}$ toward the seafloor below 150 mab, even if real, is similarly at least an order of magnitude too small to impact mean buoyancy flux. A 1D treatment simply does not explain the observed upwelling.

We suggest that the upwelling process near sloping bottoms occurs instead through an intrinsically 3D process involving strong lateral motions, which involves a rapid exchange of fluid with the interior ocean. Such exchange has been observed in other canyons (McPhee-Shaw 2006) as well as in the present canyon (Wynne-Cattanach et al. 2024). That is, upwelling happens in a rectified process wherein parcels each tidal cycle are swept in contact with the bottom, where they mix and upwell vigorously because the only water nearby is warmer—than they get swept into the interior.

Though not a complete explanation, we do note that the numerical simulation of Winters (2015), which was close in parameter space to the BLT canyon, qualitatively reproduces many of the features we observe in our dataset including diapycnal upwelling. Specifically, close examination of Fig. 1 in Winters (2015) shows that the domain is warming even though turbulence in the model increases toward the seafloor. Though it could be that the model is not yet in steady state for other reasons, the rate of warming is consistent with upwelling at a similar rate to that observed by Wynne-Cattanach et al. (2024). That is, the model did not have a deep water inflow, but the water was warming at a rate that would have balanced the inflow had it been present. We suggest that more similarly resolved simulations be conducted to investigate the detailed 3D processes that affect upwelling.

The observed tendency for $\hat{\Gamma}$ to increase toward the seafloor appears consistent with past observations using the O80

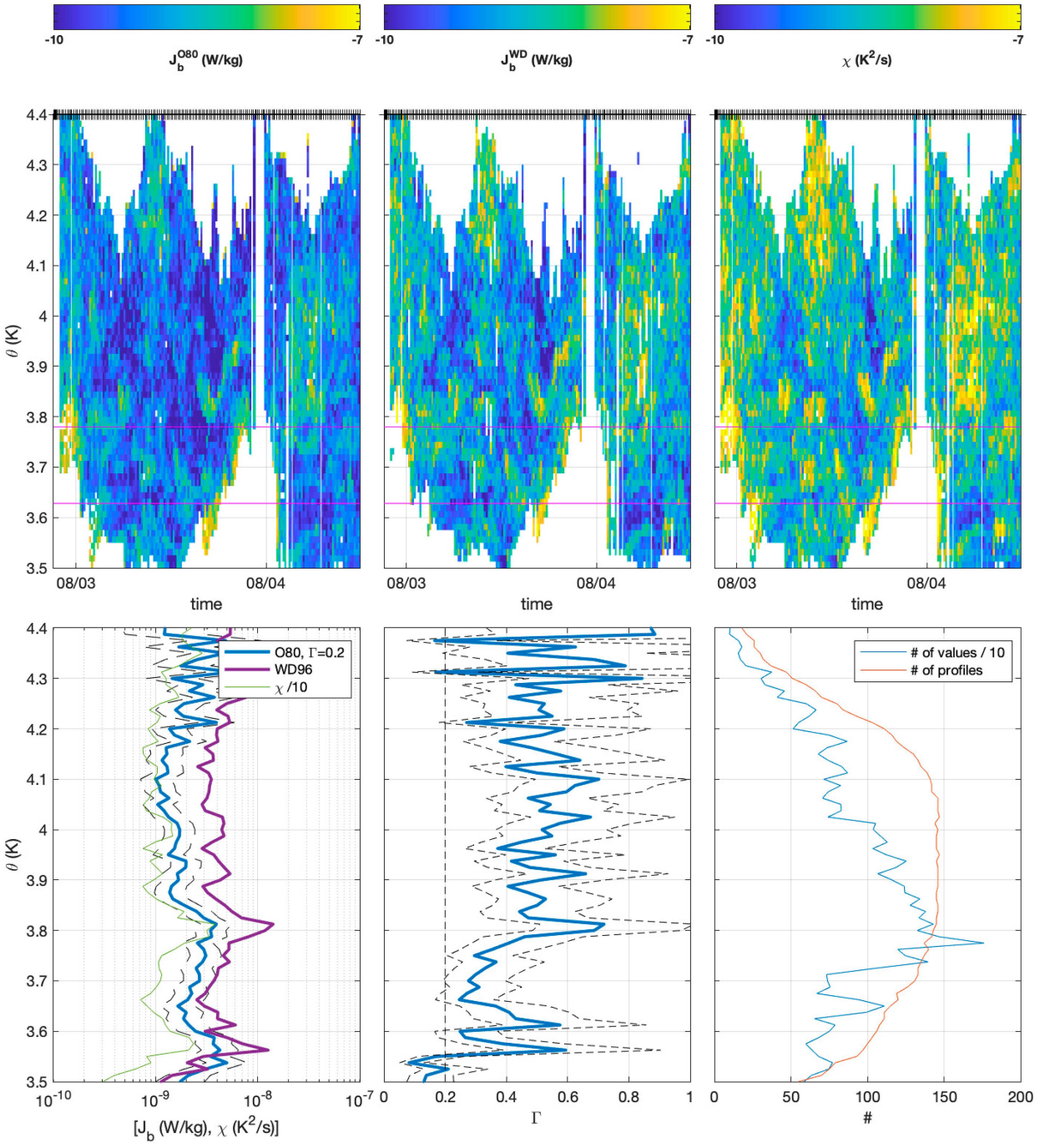

FIG. 16. As Fig. 15, but for station 7.

and OC72 methods to estimate $\hat{\Gamma}$ (Ijichi et al. 2020), who argued that the increase could indicate greater convective instability near the bottom. Since we have demonstrated that convective instability is in fact occurring in the bottom 100 m in our data, we find this explanation plausible. The additional finding that $\hat{\Gamma}$ remains 0.4–0.5 aloft at the station atop the near-critical slope is intriguing, but unfortunately cannot be confirmed in our data as we have only one station. It may be fruitful to return to numerical simulations of breaking over critical slopes such as Slinn and Riley (1996) in order to determine whether increased Γ is expected over critical slopes.

In a separate work, we will use our densely sampled data to test theoretical predictions of the evolution of J_b and Γ with "overturn age" or time since the instability that led to the turbulence. Here, we instead present a simple suggestive plot that $\hat{\Gamma}$ may depend on the tidal phase. In Fig. 19, J_b and ϵ (top) and

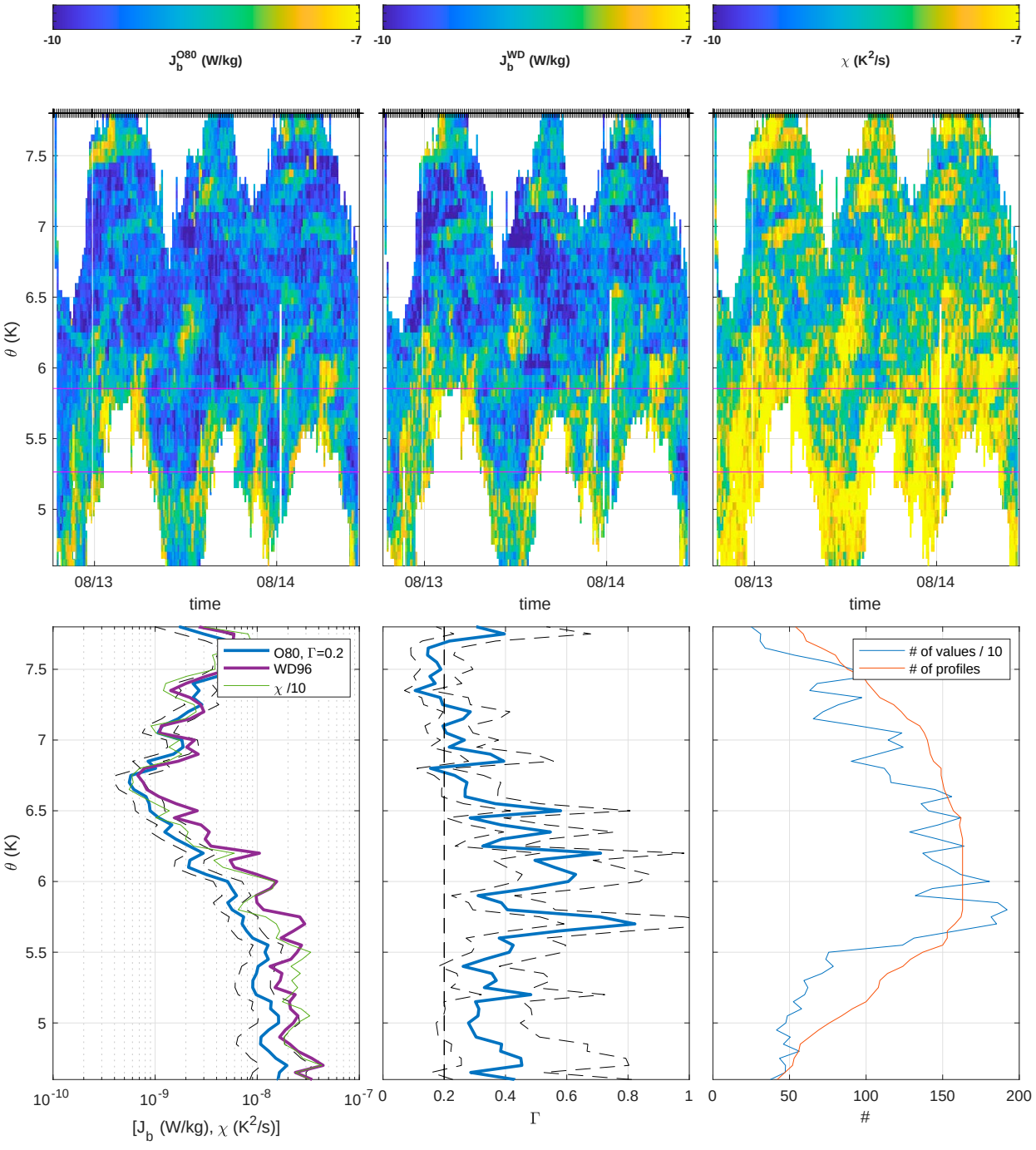

FIG. 17. As Fig. 15, but for station 12.

$\hat{\Gamma}$ (bottom) are calculated for station 12 by averaging between the 6° and 6.5° isotherms, where time-mean Γ is approximately constant in depth. In this first attempt of which we are aware to calculate a time series of the mixing efficiency, suggestive variability is present, with $\hat{\Gamma}$ varying from ~0.2 to 0.8. A hint of the tendency for the strongest turbulence to be the most efficient [so-called Goldilocks turbulence; Mashayek et al. (2021)] is seen, but more analysis is needed.

Although we have applied the recipe in WD96 section 7 exactly, we nonetheless note two limitations of its application to real microstructure datasets. First, WD96 points out that the *N*-profile averages converge to the full volume averages as *N* goes to infinity. However, because the sorting in WD96 is

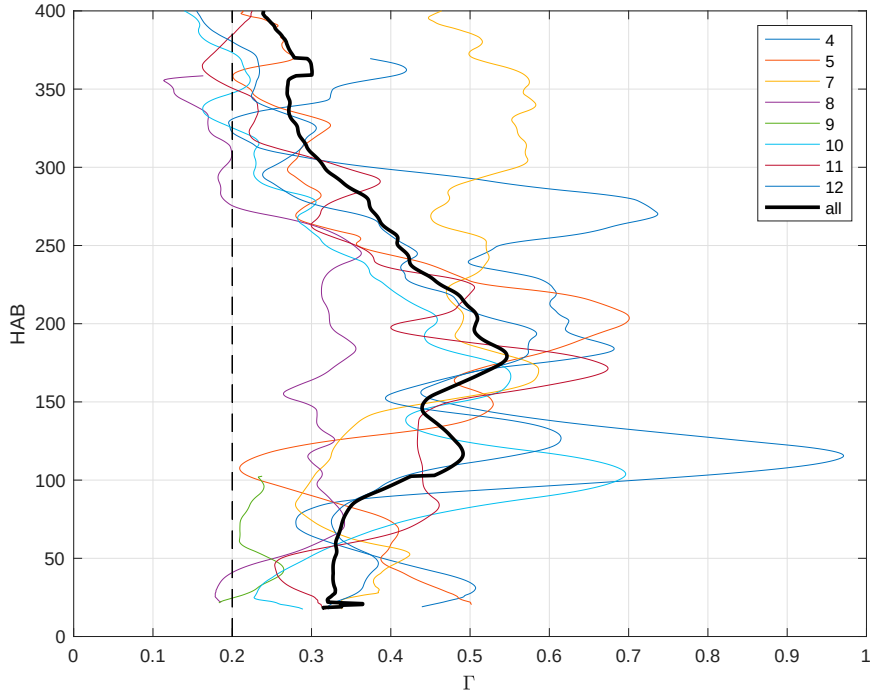

FIG. 18. The $\hat{\Gamma}$ versus height above bottom for all stations (colors) and for the mean over all stations (thick black). Error bars differ by station, but are similar to those plotted in Figs. 15–17.

assumed to be done to a snapshot, this is not strictly true if the N profiles contain time variability. In that case, some variability between isosurfaces may be due to temporal changes rather than diascalar fluxes. Though our data are less affected by this issue than most microstructure datasets because we flow the flow to a degree, we acknowledge it as a possible source of error in our technique. Second, in regions where isotherms are nearly vertical or inverted such as ours, it is asserted, rather than having been demonstrated, that the method of determining z^* from the N-profile average of θ converges. The percentage of our records that are inverted $\mathcal{O}$ (10%–20%) is large compared to datasets in regions where convective instability is not happening, but we believe that it is nonetheless small enough for our averages to converge. A future study will apply these techniques to subsampled model data to determine the limitations.

We conclude with a final caveat. One aim of this work has been to estimate the mixing efficiency as a function of height

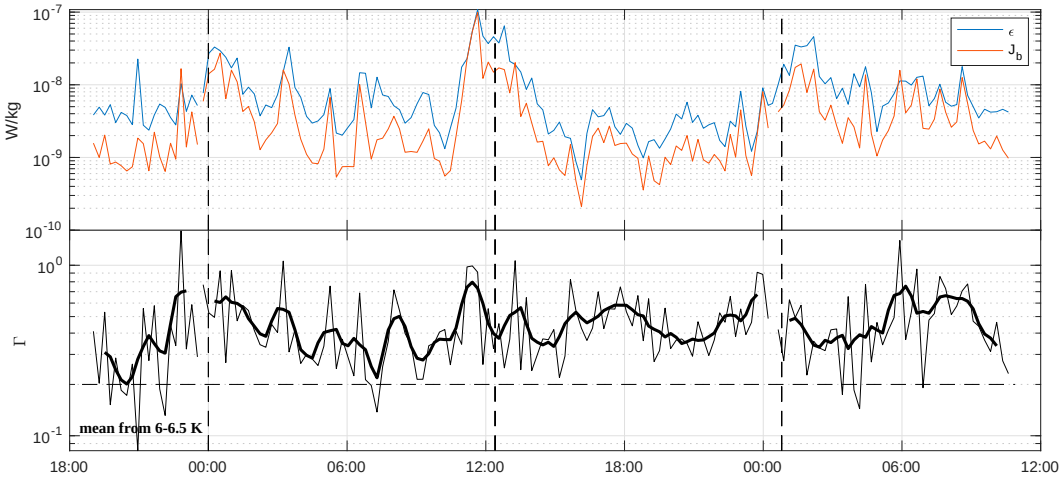

FIG. 19. The (top) ϵ and (bottom) $\hat{\Gamma}$ versus time for station 12, averaged over 6°–6.5° isotherms. The heavy line in the lower panel is a centered hourly running mean. Vertical dashed lines in both panels indicate a 12.4-h semidiurnal tidal period.

above bottom in order to examine the possibility that turbulence is less efficient near the bottom, presumably owing to the reduced stratification predicted by time-invariant models, but the same strongly advecting "internal swash" that leads to strong boundary/interior exchange also complicates this simple goal, even for our data which were often within 15 m from the bottom. That is, an examination of the isotherm records during a typical 12-h station (e.g., Figs. 8–10) shows that water parcels trace out energetic excursions into and out of the bottom boundary. It is important to recall this when interpreting Fig. 18 which plots $\hat{\Gamma}$ versus the mean height above bottom averaged over a tidal cycle: Water parcels sweep through a large range of height above bottom, turbulence intensity, and stratification during any tidal cycle. A second aspect of this caveat is that, particularly close to the bottom, the strong tidal displacements mean that some isotherms are not present for the entire tidal cycle as they are swept below our records. As such, the truly near-bed dynamics expected in the lower few meters (van Haren et al. 2024) are at best partially resolved in our profiler data. The impact of this incomplete sampling is unknown.

Acknowledgments. The authors wish to acknowledge the talent and skill of the captain, crew, and technicians aboard the RRS Discovery and the warmth and kindness with which we were received on board. This work was supported by the U.S. National Science Foundation under Award OCE-1756324 and the U.K. National Environmental Research Council under Award NE/S001433/1. We also thank the engineers of the Multiscale Ocean Dynamics group for their hard work and brilliance in developing the epsi-fish profiler, as well as the giants on whose shoulders we stand, Mike Gregg (APL/UW) and Rob Pinkel (Scripps), for their pioneering work on earlier versions of the profilers and the winch. We also thank Kurt Polzin and Raf Ferrari for many stimulating conversations and Eric D'Asaro and three anonymous reviewers for their very insightful reviews that greatly improved the manuscript.

Data availability statement. All presented data are available at our project's repository at https://doi.org/10.17882/98178.

APPENDIX

Buoyancy Fluxes When Salinity Contributions Are Nonnegligible

Because salinity microstructure is extremely hard to measure, buoyancy fluxes from OC72 or WD96 are computed using measurements of thermal dissipation rate χ via (5). However, when salinity contributes nonnegligibly to density (say $R_\rho < 10$), an additional term $-g\beta\langle w'S'\rangle$ must be included. It can be simply shown (Nash and Moum 1999, 2002) that if heat and salt turbulently diffuse downgradient at the same rate $\kappa_S = \kappa_T$, then

$$\chi_S = \left(\frac{dS}{d\theta}\right)^2 \chi. \tag{A1}$$

In that case, the total buoyancy flux including salinity fluxes, in a double diffusively stable profile, equals

$$J_b^{\text{tot}} = (1 - R_\rho^{-1}) J_b^T, \tag{A2}$$

where J_b^T is the temperature-only buoyancy flux computed using (5) and (6). All estimates of buoyancy flux from thermal dissipation rate χ, and any resulting estimates of $\hat{\Gamma}$, are subject to this potential high bias due to unmeasured salinity fluxes. For our values of $R_\rho = 2.5$–5, (eqn:jbs) indicates that J_b^T would be high by 40% and 20%, respectively. However, while we would expect $\kappa_T = \kappa_S$ for very strong turbulence, numerical simulations (Gargett 2003; Gargett et al. 2003; Smyth et al. 2005) have found $\kappa_S < \kappa_T$ for buoyancy Reynolds numbers < 100, which is physically sensible since mixing events that do not go to completion may not persist for sufficient time to allow the much slower molecular salt fluxes to fully act.

The only direct measurements of χ_S and κ_S are by Nash and Moum (1999, 2002) and Alford et al. (2006), using closely mounted microconductivity sensors and a fiber-optic refractometer, respectively. Nash and Moum (1999) found $\kappa_S = 0.75\kappa_T$, while Nash and Moum (2002) found $\kappa_S = (0.6\text{–}1.1)\kappa_T$, respectively. The term $\kappa_S < \kappa_T$ does reduce the high bias (e.g., $\kappa_S = 0.75\kappa_T$ reduces the overestimation for $R_\rho = 2.5$ from 40% to 30%), but enough uncertainty remains that we simply note the potential for bias and the associated complications rather than attempt to correct for it.

At the end of the day, salinity fluxes were not measured in our experiment and hence are unaccounted for. Hence, we acknowledge a worst-case high bias of our Γ estimates due to this effect of 40% and a possible worst-case trend in $\hat{\Gamma}$ of 12%(=1.4/1.25) over the full-depth range of our measurements due to the variations in R_ρ.

REFERENCES

Alford, M. H., and R. Pinkel, 2000: Observations of overturning in the thermocline: The context of ocean mixing. *J. Phys. Oceanogr.*, **30**, 805–832, https://doi.org/10.1175/1520-0485(2000)030<0805:OOOITT>2.0.CO;2.

——, and P. MacCready, 2014: Flow and mixing in Juan de Fuca Canyon, Washington. *Geophys. Res. Lett.*, **41**, 1608–1615, https://doi.org/10.1002/2013GL058967.

——, D. W. Gerdt, and C. M. Adkins, 2006: An ocean refractometer: Resolving millimeter-scale turbulent density fluctuations via the refractive index. *J. Atmos. Oceanic Technol.*, **23**, 121–137, https://doi.org/10.1175/JTECH1830.1.

——, and Coauthors, 2011: Energy flux and dissipation in Luzon Strait: Two tales of two ridges. *J. Phys. Oceanogr.*, **41**, 2211–2222, https://doi.org/10.1175/JPO-D-11-073.1.

Armi, L., 1978: Some evidence for boundary mixing in the deep ocean. *J. Geophys. Res.*, **83**, 1971–1979, https://doi.org/10.1029/JC083iC04p01971.

Batchelor, G. K., 1967: *An Introduction to Fluid Dynamics.* 1st ed. Cambridge University Press, 615 pp.

Cael, B. B., and A. Mashayek, 2021: Log-skew-normality of ocean turbulence. *Phys. Rev. Lett.*, **126**, 224502, https://doi.org/10.1103/PhysRevLett.126.224502.

Chor, T., J. O. Wenegrat, and J. Taylor, 2022: Insights into the mixing efficiency of submesoscale centrifugal–symmetric instabilities. *J. Phys. Oceanogr.*, **52**, 2273–2287, https://doi.org/10.1175/JPO-D-21-0259.1.

Cimoli, L., C.-c. P. Caulfield, H. L. Johnson, D. P. Marshall, A. Mashayek, A. C. Naveira Garabato, and C. Vic, 2019: Sensitivity of deep ocean mixing to local internal tide breaking and mixing efficiency. *Geophys. Res. Lett.*, **46**, 14 622–14 633, https://doi.org/10.1029/2019GL085056.

Cyr, F., and H. Van Haren, 2016: Observations of small-scale secondary instabilities during the shoaling of internal bores on a deep-ocean slope. *J. Phys. Oceanogr.*, **46**, 219–231, https://doi.org/10.1175/JPO-D-15-0059.1.

Dalziel, S. B., M. D. Patterson, C. P. Caulfield, and I. A. Coomaraswamy, 2008: Mixing efficiency in high-aspect-ratio Rayleigh–Taylor experiments. *Phys. Fluids*, **20**, 065106, https://doi.org/10.1063/1.2936311.

de Lavergne, C., G. Madec, J. Le Sommer, A. J. G. Nurser, and A. C. Naveira Garabato, 2016: The impact of a variable mixing efficiency on the abyssal overturning. *J. Phys. Oceanogr.*, **46**, 663–681, https://doi.org/10.1175/JPO-D-14-0259.1.

Dillon, T. M., 1982: Vertical overturns: A comparison of Thorpe and Ozmidov length scales. *J. Geophys. Res.*, **87**, 9601–9613, https://doi.org/10.1029/JC087iC12p09601.

Ferrari, R., A. Mashayek, T. J. McDougall, M. Nikurashin, and J.-M. Campin, 2016: Turning ocean mixing upside down. *J. Phys. Oceanogr.*, **7**, 2239–2261, https://doi.org/10.1175/JPO-D-15-0244.1.

Gargett, A. E., 2003: Differential diffusion: An oceanographic primer. *Prog. Oceanogr.*, **56**, 559–570, https://doi.org/10.1016/S0079-6611(03)00025-9.

——, W. J. Merryfield, and G. Holloway, 2003: Direct numerical simulation of differential scalar diffusion in three-dimensional stratified turbulence. *J. Phys. Oceanogr.*, **33**, 1758–1782, https://doi.org/10.1175/2403.1.

Garrett, C., 1979: Comment on 'some evidence for boundary mixing in the deep ocean' by Laurence Armi. *J. Geophys. Res.*, **84**, 5095, https://doi.org/10.1029/JC084iC08p05095.

——, 2001: An isopycnal view of near-boundary mixing and associated flows. *J. Phys. Oceanogr.*, **31**, 138–143, https://doi.org/10.1175/1520-0485(2001)031<0138:AIVONB>2.0.CO;2.

Gayen, B., G. O. Hughes, and R. W. Griffiths, 2013: Completing the mechanical energy pathways in turbulent Rayleigh-Bénard convection. *Phys. Rev. Lett.*, **111**, 124301, https://doi.org/10.1103/PhysRevLett.111.124301.

Gregg, M. C., 1989: Scaling turbulent dissipation in the thermocline. *J. Geophys. Res.*, **94**, 9686–9698, https://doi.org/10.1029/JC094iC07p09686.

——, and T. B. Meagher, 1980: The dynamic response of glass rod thermistors. *J. Geophys. Res.*, **85**, 2779–2786, https://doi.org/10.1029/JC085iC05p02779.

——, H. E. Seim, and D. Percival, 1993: Statistics of shear and turbulent dissipation profiles in random internal wave fields. *J. Phys. Oceanogr.*, **23**, 1777–1799, https://doi.org/10.1175/1520-0485(1993)023<1777:SOSATD>2.0.CO;2.

——, E. A. D'Asaro, J. J. Riley, and E. Kunze, 2018: Mixing efficiency in the ocean. *Annu. Rev. Mar. Sci.*, **10**, 443–473, https://doi.org/10.1146/annurev-marine-121916-063643.

Gurvich, A. S., and A. M. Yaglom, 1993: Breakdown of eddies and probability distributions for small-scale turbulence. *Phys. Fluids*, **10**, 59–65, https://doi.org/10.1063/1.1762505.

Hayes, S. P., H. B. Milburn, and E. F. Ford, 1984: TOPS: A free-fall velocity and CTD profiler. *J. Atmos. Oceanic Technol.*, **1**, 220–236, https://doi.org/10.1175/1520-0426(1984)001<0220:TAFFVA>2.0.CO;2.

Hosegood, P., H. van Haren, and C. Veth, 2005: Mixing within the interior of the Faeroe-Shetland channel. *J. Mar. Res.*, **63**, 529–561, https://doi.org/10.1357/0022240054307902.

Ijichi, T., and T. Hibiya, 2018: Observed variations in turbulent mixing efficiency in the deep ocean. *J. Phys. Oceanogr.*, **48**, 1815–1830, https://doi.org/10.1175/JPO-D-17-0275.1.

——, L. St. Laurent, K. L. Polzin, and J. M. Toole, 2020: How variable is mixing efficiency in the abyss? *Geophys. Res. Lett.*, **47**, e2019GL086813, https://doi.org/10.1029/2019GL086813.

Klymak, J. M., R. Pinkel, and L. Rainville, 2008: Direct breaking of the internal tide near topography: Kaena Ridge, Hawaii. *J. Phys. Oceanogr.*, **38**, 380–399, https://doi.org/10.1175/2007JPO3728.1.

Kraichnan, R. H., 1968: Small-scale structure of a scalar field convected by turbulence. *Phys. Fluids*, **11**, 945–953, https://doi.org/10.1063/1.1692063.

Kunze, E., C. MacKay, E. E. McPhee-Shaw, K. Morrice, J. B. Girton, and S. R. Terker, 2012: Turbulent mixing and exchange with interior waters on sloping boundaries. *J. Phys. Oceanogr.*, **42**, 910–927, https://doi.org/10.1175/JPO-D-11-075.1.

Le Boyer, A., and Coauthors, 2021: Modular, flexible, low-cost microstructure measurements: The epsilometer. *J. Atmos. Oceanic Technol.*, **38**, 657–668, https://doi.org/10.1175/JTECH-D-20-0116.1.

Ledwell, J. R., A. J. Watson, and C. S. Law, 1993: Evidence for slow mixing across the pycnocline from an open-ocean tracer-release experiment. *Nature*, **364**, 701–703, https://doi.org/10.1038/364701a0.

Lee, I.-H., R.-C. Lien, J. T. Liu, and W. s. Chuang, 2009: Turbulent mixing and internal tides in Gaoping (Kaoping) Submarine Canyon, Taiwan. *J. Mar. Syst.*, **76**, 383–396, https://doi.org/10.1016/j.jmarsys.2007.08.005.

Levine, M. D., and T. J. Boyd, 2006: Tidally forced internal waves and overturns observed on a slope: Results from HOME. *J. Phys. Oceanogr.*, **36**, 1184–1201, https://doi.org/10.1175/JPO2887.1.

Lorke, A., F. Peeters, and A. Wüest, 2005: Shear-induced convective mixing in bottom boundary layers on slopes. *Limnol. Oceanogr.*, **50**, 1612–1619, https://doi.org/10.4319/lo.2005.50.5.1612.

Lueck, R., and Coauthors, 2024: Best practices recommendations for estimating dissipation rates from shear probes. *Front. Mar. Sci.*, **11**, 1334327, https://doi.org/10.3389/fmars.2024.1334327.

Mashayek, A., C. P. Caulfield, and M. H. Alford, 2021: Goldilocks mixing in oceanic shear-induced turbulent overturns. *J. Fluid Mech.*, **928**, A1, https://doi.org/10.1017/jfm.2021.740.

Mater, B. D., S. M. Schaad, and S. K. Venayagamoorthy, 2013: Relevance of the Thorpe length scale in stably stratified turbulence. *Phys. Fluids*, **25**, 076604, https://doi.org/10.1063/1.4813809.

——, S. K. Venayagamoorthy, L. S. Laurent, and J. N. Moum, 2015: Biases in Thorpe scale estimates of turbulence dissipation. Part I: Assessments from large-scale overturns in oceanographic data. *J. Phys. Oceanogr.*, **45**, 2497–2521, https://doi.org/10.1175/JPO-D-14-0128.1.

McDougall, T. J., and R. Ferrari, 2017: Abyssal upwelling and downwelling driven by near-boundary mixing. *J. Phys. Oceanogr.*, **47**, 261–283, https://doi.org/10.1175/JPO-D-16-0082.1.

McPhee-Shaw, E., 2006: Boundary–interior exchange: Reviewing the idea that internal-wave mixing enhances lateral dispersal near continental margins. *Deep-Sea Res. II*, **53**, 42–59, https://doi.org/10.1016/j.dsr2.2005.10.018.

Monismith, S. G., J. R. Koseff, and B. L. White, 2018: Mixing efficiency in the presence of stratification: When is it constant? *Geophys. Res. Lett.*, **45**, 5627–5634, https://doi.org/10.1029/2018GL077229.

Moum, J. N., 1996: Efficiency of mixing in the main thermocline. *J. Geophys. Res.*, **101**, 12 057–12 069, https://doi.org/10.1029/96JC00508.

——, D. R. Caldwell, J. D. Nash, and G. D. Gunderson, 2002: Observations of boundary mixing over the continental slope. *J. Phys. Oceanogr.*, **32**, 2113–2130, https://doi.org/10.1175/1520-0485(2002)032<2113:OOBMOT>2.0.CO;2.

——, A. Perlin, J. M. Klymak, M. D. Levine, T. Boyd, and P. M. Kosro, 2004: Convectively driven mixing in the bottom boundary layer. *J. Phys. Oceanogr.*, **34**, 2189–2202, https://doi.org/10.1175/1520-0485(2004)034<2189:CDMITB>2.0.CO;2.

Munk, W., and C. Wunsch, 1998: Abyssal recipes II: Energetics of tidal and wind mixing. *Deep-Sea Res. I*, **45**, 1977–2010, https://doi.org/10.1016/S0967-0637(98)00070-3.

Munk, W. H., 1966: Abyssal recipes. *Deep-Sea Res. Oceanogr. Abstr.*, **13**, 707–730, https://doi.org/10.1016/0011-7471(66)90602-4.

Nash, J. D., and J. N. Moum, 1999: Estimating salinity variance dissipation rate from conductivity microstructure measurements. *J. Atmos. Oceanic Technol.*, **16**, 263–274, https://doi.org/10.1175/1520-0426(1999)016<0263:ESVDRF>2.0.CO;2.

——, and ——, 2002: Microstructure estimates of turbulent salinity flux and the dissipation spectrum of salinity. *J. Phys. Oceanogr.*, **32**, 2312–2334, https://doi.org/10.1175/1520-0485(2002)032<2312:MEOTSF>2.0.CO;2.

Nasmyth, P. W., 1970: Oceanic turbulence. Ph.D. thesis, University of British Columbia, 69 pp.

Osborn, T. R., 1980: Estimates of the local rate of vertical diffusion from dissipation measurements. *J. Phys. Oceanogr.*, **10**, 83–89, https://doi.org/10.1175/1520-0485(1980)010<0083:EOTLRO>2.0.CO;2.

——, and C. S. Cox, 1972: Oceanic fine structure. *Geophys. Fluid Dyn.*, **3**, 321–345, https://doi.org/10.1080/03091927208236085.

Peterson, A. K., and I. Fer, 2014: Dissipation measurements using temperature microstructure from an underwater glider. *Methods Oceanogr.*, **10**, 44–69, https://doi.org/10.1016/j.mio.2014.05.002.

Petruncio, E. T., L. K. Rosenfeld, and J. D. Paduan, 1998: Observations of the internal tide in Monterey Canyon. *J. Phys. Oceanogr.*, **28**, 1873–1903, https://doi.org/10.1175/1520-0485(1998)028<1873:OOTITI>2.0.CO;2.

Pinkel, R., J. Sherman, J. Smith, and S. Anderson, 1991: Strain: Observations of the vertical gradient of isopycnal vertical displacement. *J. Phys. Oceanogr.*, **22**, 527–540, https://doi.org/10.1175/1520-0485(1991)021<0527:SOOTVG>2.0.CO;2.

Polzin, K. L., 2009: An abyssal recipe. *Ocean Modell.*, **30**, 298–309, https://doi.org/10.1016/j.ocemod.2009.07.006.

——, and T. J. McDougall, 2022: Mixing at the ocean's bottom boundary. *Ocean Mixing*, Elsevier, 145–180, https://doi.org/10.1016/B978-0-12-821512-8.00014-1.

——, J. M. Toole, J. R. Ledwell, and R. W. Schmitt, 1997: Spatial variability of turbulent mixing in the abyssal ocean. *Science*, **276**, 93–96, https://doi.org/10.1126/science.276.5309.93.

——, B. Wang, Z. Wang, F. Thwaites, and A. J. Williams III, 2021: Moored flux and dissipation estimates from the northern deepwater Gulf of Mexico. *Fluids*, **6**, 237, https://doi.org/10.3390/fluids6070237.

Ruan, X., A. F. Thompson, and J. R. Taylor, 2019: The evolution and arrest of a turbulent stratified oceanic bottom boundary layer over a slope: Downslope regime. *J. Phys. Oceanogr.*, **49**, 469–487, https://doi.org/10.1175/JPO-D-18-0079.1.

Shay, T. J., and M. C. Gregg, 1984: Turbulence in an oceanic convective mixed layer. *Nature*, **310**, 282–285, https://doi.org/10.1038/310282a0.

Simpson, J. H., J. Brown, J. Matthews, and G. Allen, 1990: Tidal straining, density currents, and stirring in the control of estuarine stratification. *Estuaries*, **13**, 125–132, https://doi.org/10.2307/1351581.

Slinn, D. N., and J. J. Riley, 1996: Turbulent mixing in the oceanic boundary layer caused by internal wave reflection from sloping terrain. *Dyn. Atmos. Oceans*, **24**, 51–62, https://doi.org/10.1016/0377-0265(95)00425-4.

Smyth, W. D., J. N. Moum, and D. R. Caldwell, 2001: The efficiency of mixing in turbulent patches: Inferences from direct simulations and microstructure observations. *J. Phys. Oceanogr.*, **31**, 1969–1992, https://doi.org/10.1175/1520-0485(2001)031<1969:TEOMIT>2.0.CO;2.

——, J. D. Nash, and J. N. Moum, 2005: Differential diffusion in breaking Kelvin–Helmholtz billows. *J. Phys. Oceanogr.*, **35**, 1004–1022, https://doi.org/10.1175/JPO2739.1.

Spingys, C. P., A. C. Naveira Garabato, S. Legg, K. L. Polzin, E. P. Abrahamsen, C. E. Buckingham, A. Forryan, and E. E. Frajka-Williams, 2021: Mixing and transformation in a deep western boundary current: A case study. *J. Phys. Oceanogr.*, **51**, 1205–1222, https://doi.org/10.1175/JPO-D-20-0132.1.

St. Laurent, L. C., J. M. Toole, and R. W. Schmitt, 2001: Buoyancy forcing by turbulence above rough topography in the abyssal Brazil Basin. *J. Phys. Oceanogr.*, **31**, 3476–3495, https://doi.org/10.1175/1520-0485(2001)031<3476:BFBTAR>2.0.CO;2.

van Haren, H., and L. Gostiaux, 2012: Detailed internal wave mixing above a deep-ocean slope. *J. Mar. Res.*, **70**, 173–197, https://doi.org/10.1357/002224012800502363.

——, G. Voet, M. H. Alford, B. Fernández-Castro, A. C. Naveira Garabato, B. L. Wynne-Cattanach, H. Mercier, and M.-J. Messias, 2024: Near-slope turbulence in a Rockall canyon. *Deep-Sea Res. I*, **206**, 104277, https://doi.org/10.1016/j.dsr.2024.104277.

Voet, G., and Coauthors, 2024: Near-inertial energy variability in a strong mesoscale eddy field in the Iceland Basin. *Oceanography*, **37**, 34–47, https://doi.org/10.5670/oceanog.2024.302.

Waterhouse, A. F., J. A. Mackinnon, R. C. Musgrave, S. M. Kelly, A. Pickering, and J. Nash, 2017: Internal tide convergence and mixing in a submarine canyon. *J. Phys. Oceanogr.*, **47**, 303–322, https://doi.org/10.1175/JPO-D-16-0073.1.

Winters, K. B., 2015: Tidally driven mixing and dissipation in the stratified boundary layer above steep submarine topography. *Geophys. Res. Lett.*, **42**, 7123–7130, https://doi.org/10.1002/2015GL064676.

——, and E. A. D'Asaro, 1996: Diascalar flux and the rate of fluid mixing. *J. Fluid Mech.*, **317**, 179–193, https://doi.org/10.1017/S0022112096000717.

Wunsch, C., and R. Ferrari, 2004: Vertical mixing, energy, and the general circulation of the oceans. *Annu. Rev. Fluid Mech.*, **36**, 281–314, https://doi.org/10.1146/annurev.fluid.36.050802.122121.

Wynne-Cattanach, B. L., and Coauthors, 2024: Observations of diapycnal upwelling within a sloping submarine canyon. *Nature*, **630**, 884–890, https://doi.org/10.1038/s41586-024-07411-2.

Copyright of Journal of Physical Oceanography is the property of American Meteorological Society and its content may not be copied or emailed to multiple sites or posted to a listserv without the copyright holder's express written permission. However, users may print, download, or email articles for individual use.